https://dx.doi.org/10.1016/j.engstruct.2022.114869

Compressive behavior and analysis-oriented model of FRP-confined engineered cementitious composite columns

Shuai Li, Tak-Ming Chan*, Ben Young

Department of Civil and Environmental Engineering, The Hong Kong Polytechnic University, Hong Kong, China

*Corresponding author.

Email address: tak-ming.chan@polyu.edu.hk (T.-M. Chan).

Abstract

A total of 18 specimens of fiber-reinforced polymer (FRP) confined engineered cementitious composite (ECC) were tested under axial compression in this study. Both monotonic loading and cyclic loading were considered. Effects of different FRP materials, glass FRP (GFRP) tube and carbon FRP (CFRP) jacket, as well as different FRP thicknesses were investigated. All the specimens exhibited the typical strain hardening behavior, indicating the effective enhancement of compressive strength and strain of ECC under FRP confinement. Failure modes, stress-strain behavior and dilation behavior were presented and analyzed. The FRP-confined ECC showed large ultimate axial strains, demonstrating the superior deformability and ductility performance. Design equations were developed to predict the ultimate compressive strength and strain. Based on the test results obtained from this study and other test results collected in the literature, an analysis-oriented model was proposed to predict the overall compressive stress-strain behavior of FRP-confined ECC columns.

Keywords: analysis-oriented model; compressive behavior; confinement; engineered cementitious composite (ECC); fiber-reinforced polymer (FRP)

Nomenclature	
c	constant in axial strain enhancement equation
D	diameter of confined ECC
E_c	elastic modulus of concrete
E_f	elastic modulus of confining FRP
f'_{c0}	compressive strength of unconfined ECC
f'^{*}_{cc}	peak axial compressive stress of actively-confined concrete
f'_{cu}	ultimate compressive strength of FRP-confined ECC
$f'_{cu,pred}$	predicted ultimate compressive strength of FRP-confined ECC
$f'_{cu,test}$	test ultimate compressive strength of FRP-confined ECC
f_l	confining pressure
$f_{lu,a}$	actual confining pressure at FRP rupture
K_l	FRP confining stiffness

k_1	axial compressive strength enhancement coefficient
k_2	axial compressive strain enhancement coefficient
r	parameter in equation of actively-confined concrete
t_f	thickness of confining FRP
ε_c	axial strain of FRP-confined concrete
ε_{c0}	axial strain corresponding to the compressive strength of unconfined ECC
ε_{cc}^*	axial strain of actively-confined concrete corresponding to $f_{cc}'^*$
ε_{cu}	ultimate axial strain of FRP-confined ECC
$\varepsilon_{cu,pred}$	predicted ultimate axial strain of FRP-confined ECC
$\varepsilon_{cu,test}$	test ultimate axial strain of FRP-confined ECC
$\varepsilon_{h,rup}$	average hoop FRP rupture strain
ε_l	lateral strain of FRP-confined concrete
σ_c	axial stress of FRP-confined concrete

1. Introduction

Concrete is one of the most commonly used constructional materials in civil engineering because of the excellent compressive behavior and relatively low cost. However, the brittle characteristic and limited tensile resistance may also lead to many challenges in concrete structures [1-3], such as concrete cover spalling and concrete cracking followed by inner steel rebar corrosion. To improve the toughness of concrete, a ductile concrete material named engineered cementitious composite (ECC) was developed [4,5]. Short polymer fibers, normally polyethylene (PE) fibers, polyvinyl alcohol (PVA) fibers or polypropylene (PP) fibers, are used and randomly distributed in ECC mixture. Compared with normal concrete, ECC can develop a ductile tensile strain hardening behavior with an obviously improved tensile strain capacity up to 10% [4,5]. When a microcrack initiates in ECC, the fiber bridging the microcrack will prevent its width to continue increasing. Meanwhile, multiple microcracks will occur with the average width in a stable state of less than 100 μm [6]. Recent research has explored the utilization of ECC in different structural forms, such as using ECC layer in the tension zone of reinforced concrete beams [7], using reinforced ECC cover to provide additional confinement in hybrid columns [8-11] and repair and strengthening with ECC in the plastic hinge zone of beam-column joints [12,13]. These applications aim to improve the deformability and ductility of the composite members with the advantages of ECC, leading to the enhanced structural performance especially under extreme loadings. It is worth noting that the composite members are normally developed by replacing partial normal concrete with ECC in the crucial regions, rather than fully cast with ECC. Because of the higher cost of ECC than normal concrete, this arrangement can achieve the effective and optimal design from the aspects of both structural behavior and economy [14].

In additional to the aforementioned advantages, there are also challenges that need to be solved for the application of ECC, such as the strain softening behavior of ECC under compressive loads [15-19]. Similar to FRP-confined normal concrete [20-23], it is an effective approach to improve the compressive strength and strain of ECC with lateral FRP confinement [24-26]. Dang et al. [24] experimentally compared the compressive behavior of ECC cylinders and normal concrete cylinders confined by FRP jackets and found that FRP-confined ECC could develop the obviously larger ultimate axial strain than FRP-confined normal concrete under the same level of confinement. It was also reported by Li et al. [26] that when adopting an annular ECC layer in the FRP-confined high strength concrete column, the hoop strain on FRP tube could be more uniform because of the multiple cracking behavior of ECC, which could help to redistribute the hoop strain and avoid strain concentration. The failure of FRP rupture was consequently delayed with the enhanced column deformability. Therefore, FRP-confined ECC has the potential to exhibit advantages over FRP-confined normal concrete under the extreme conditions, such as seismic loadings where the structural members are required to withstand relatively large deformations. Cyclic compression is of particular interest when seismic loadings are considered for structural columns. Dang et al. [24] reported the cyclic compressive behavior of FRP-confined ECC and noted that the cyclically loaded specimens tended to achieve relatively larger compressive strength and strain. Meanwhile, the upper boundary of the cyclic stress-strain curve was found to be close to the monotonic stress-strain curve for FRP-confined ECC.

For FRP-confined normal concrete, there have been extensive studies presenting the analysis and design-oriented models [27,28]. For FRP-confined ECC, Dang et al. [24] proposed the design equations of ultimate conditions and noted that the strength enhancement coefficient was different from that for FRP-confined normal concrete. Meanwhile, Yuan et al. [25] proposed the lateral strain-axial strain model for FRP-confined ECC and revealed that the dilation behavior of FRP-confined ECC was different from that of FRP-confined normal concrete due to the self-confinement effect of ECC. Since the dilation of confined concrete is highly related to the confining pressure [27,28], it may lead to that the existing analysis and design models developed based on FRP-confined normal concrete cannot provide accurate predictions on the stress-strain behavior of FRP-confined ECC. In the current stage, research on the compressive behavior of FRP-confined ECC is relatively limited. It is worthwhile to carry out more experimental investigations under both monotonic and cyclic loadings to enrich the test database.

Analysis and design models that are applicable to FRP-confined ECC need to be proposed based on the enlarged test database. The models are useful not only for FRP-confined solid ECC columns, but also for various FRP-confined concrete composite members wherever ECC is adopted.

In this study, experimental investigations on FRP-confined ECC columns under both monotonic and cyclic loadings were conducted to fully understand the compressive behavior. Failure modes, stress-strain responses and dilation behavior were carefully presented and analyzed. Design equations were developed to predict the ultimate compressive strength and ultimate axial strain. Based on the test results obtained from this study and other test results collected from literature, an analysis-oriented model was proposed to predict the overall compressive stress-strain behavior of FRP-confined ECC columns.

2. Experimental investigation

2.1 Material properties

2.1.1 ECC

ECC mix proportions are given in Table 1. 2% volume of polyethylene (PE) fiber, with the properties provided in Table 2, was used in the ECC mixture. Three 100 mm × 200 mm cylinders were cast together with the FRP-confined ECC specimens and used to determine the compressive properties of plain ECC. According to test standards ASTM C39 [29] and ASTM C469 [30], the stress loading rate of 0.3 MPa/s was adopted for the compression tests, which yielded the equivalent displacement loading rate of 0.24 mm/min under the displacement-controlled loading method. Strain gauges and LVDTs were used to monitor the compressive strain. Axial load would drop after reaching the ECC compressive strength and the loading was stopped when the residual load was 25% that of the peak load. Compressive stress-strain curves for plain ECC cylinders are plotted in Fig. 1. Compressive strength, axial strain corresponding to the compressive strength and elastic modulus are 40.0 MPa, 0.0041 and 15.0 GPa, respectively. Poisson’s ratio was calculated to be 0.21.

Direct tensile tests were also carried out on three ECC coupons as per the recommendations of JSCE [31] to obtain the tensile behavior of ECC. Displacement-controlled loading method, with the displacement loading rate of 0.5 mm/min, was adopted for the tensile tests as suggested by JSCE [31]. LVDTs were used to measure the tensile strain. The tensile load would fluctuate during the formation of cracks and the loading was stopped when the axial strain reached 6% in the post-peak stage. Tensile stress-strain curves as well as the typical failed specimen are presented in Fig. 2. ECC coupons exhibited the ductile tensile behavior and multiple fine cracking behavior, with the tensile strength of 4.9 MPa and tensile strain capacity of 3.8%.

Table 1 ECC mix proportions (kg/m^3)

Concrete	Water	Cement	Fly ash	Sand	S.P.*	Fiber
ECC	320.0	550.0	660.0	460.0	13.5	19.4

S.P.*: Super plasticizer.

Table 2 Polyethylene (PE) fiber properties

Diameter (μm)	Length (mm)	Density (g/cm^3)	Elastic modulus (GPa)	Tensile strength (MPa)
24	12	0.97	120	3000

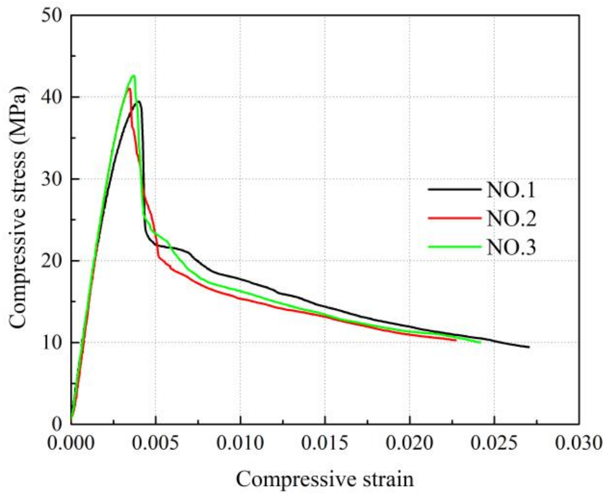

Fig. 1 Compressive stress-strain behavior of ECC

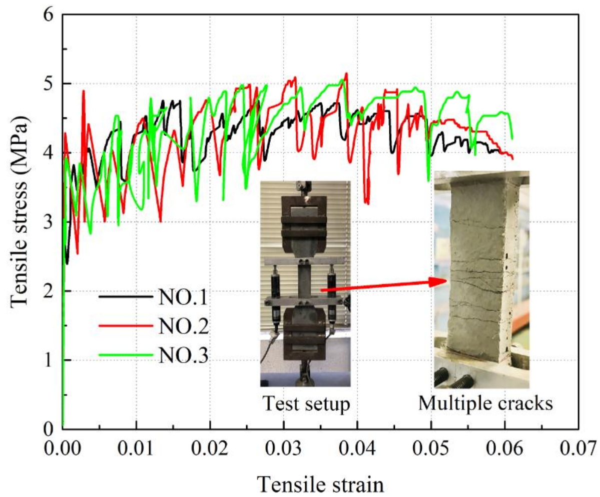

Fig. 2 Tensile stress-strain behavior of ECC

2.1.2 FRP

Two different FRP materials, glass FRP (GFRP) tube and carbon FRP (CFRP) jacket, were used in this study to provide confinement for ECC. GFRP tube was manufactured by filament winding process, with the fiber orientation of 80 degree with respect to the longitudinal axis. Five FRP rings with the width of 50 mm were cut from the GFRP tube for split-disk tests as per ASTM D2290-08 standard [32]. Four strain gauges were installed on the outer surface of the FRP ring and kept 15 mm away from the gap between the two semi-circular disks for tensile strain measurement. Tensile properties of GFRP tube are obtained and presented in Table 3. Five tensile coupons with the width of 15 mm and length of 250 mm were prepared and tested for CFRP jacket according to the requirements of ASTM D3039-17 [33]. Steel plates with the width of 15 mm and length of 56 mm were bonded at the two ends of the coupons with epoxy to transfer load and avoid local failure when clamped to the machine grips. Two strain gauges were attached at the mid-length of both sides of the coupon for strain measurement. Tensile properties of CFRP jacket are presented in Table 3.

Table 3 Tensile properties of FRP materials

FRP material	Elastic modulus (GPa)	Tensile strength (MPa)	Ultimate tensile strain

GFRP tube	39.2	626.4	0.0160
CFRP jacket	255.0	4200.2	0.0179

2.2 Test specimens

A total of 18 FRP-confined ECC specimens were prepared and tested under axial monotonic and cyclic compression. The cylindrical specimens had two nominal diameters, which were 100 mm and 200 mm, with the corresponding heights of 200 mm and 400mm. The height to diameter ratio is 2 for the tested specimens in this study, which is widely adopted for stub columns to investigate the structural behavior under pure axial compression [22-25,34]. All the specimens are listed in Table 4. For the specimen label, "G" and "C" refer to GFRP tube and CFRP jacket respectively; "6", "7", "8" and "10" stand for 6, 7, 8 and 10 filament winding layers for the GFRP tube; "2" and "4" stand for 2 and 4 wrapping layers of CFRP jacket; "M1" and "M2" represent the two identical specimens under monotonic loading, while "C" represents the specimen under cyclic loading. For GFRP tube confined ECC specimens, ECC was cast into the prepared GFRP tubes. For CFRP jacket confined ECC specimens, ECC cylinders were firstly cast, followed by CFRP jacket wrapping in the circumferential direction with epoxy resin through the wet lay-up process. An overlapping zone with the length of 100 mm was adopted for all the wrapped specimens to ensure the continuity of CFRP jacket and adequate bonding. Two end surfaces of the column were carefully capped using high strength gypsum material to ensure the specimen was in full contact with the loading plates.

Table 4 Details and key results of tested specimens

Specimen label	FRP type	D (mm)	t_f (mm)	f'_{cu} (MPa)	ε_{cu}	$\varepsilon_{h,rup}$	$f_{lu,a}$ (MPa)	$f_{lu,a}/f'_{c0}$
G-6-M1	GFRP tube	100	2.00	99.2	0.0713	0.0180	28.2	0.71
G-6-M2	GFRP tube	100	2.00	105.2	0.0746	0.0188	29.5	0.74
G-6-C	GFRP tube	100	2.00	136.5	0.1025	0.0220	34.5	0.86
G-8-M1	GFRP tube	100	2.45	114.6	0.0815	0.0192	36.9	0.92
G-8-M2	GFRP tube	100	2.45	113.5	0.0849	0.0185	35.5	0.89
G-8-C	GFRP tube	100	2.45	113.3	0.0913	0.0190	36.5	0.91
G-7-M1	GFRP tube	200	2.35	56.9	0.0266	0.0119	11.0	0.27
G-7-M2	GFRP tube	200	2.35	60.0	0.0272	0.0123	11.3	0.28
G-7-C	GFRP tube	200	2.35	56.8	0.0332	0.0145	13.4	0.33
G-10-M1	GFRP tube	200	3.45	85.0	0.0518	0.0141	19.1	0.48
G-10-M2	GFRP tube	200	3.45	84.6	0.0493	0.0140	18.9	0.47
G-10-C	GFRP tube	200	3.45	84.6	0.0555	0.0149	20.2	0.50
C-2-M1	CFRP jacket	100	0.22	73.2	0.0507	0.0178	20.0	0.50
C-2-M2	CFRP jacket	100	0.22	77.1	0.0616	0.0182	20.4	0.51
C-2-C	CFRP jacket	100	0.22	77.0	0.0587	0.0155	17.4	0.43
C-4-M1	CFRP jacket	100	0.44	192.4	0.1410	0.0238	53.4	1.34
C-4-M2	CFRP jacket	100	0.44	130.8	0.0937	0.0183	41.1	1.03

C-4-C	CFRP jacket	100	0.44	198.5	0.1418	0.0228	51.2	1.28

2.3 Test setup and loading

Axial compression tests were conducted on the MTS 815 rock mechanics system. Fig. 3 shows the test setup and specimen instrumentations. Strain gauges with the gauge length of 5 mm were installed on the GFRP tube or CFRP jacket surface in the mid-height of the specimen in the hoop direction for hoop strain measurements. Eight hoop strain gauges at every 45° were used for the specimens with the diameter of 100 mm, while twelve hoop strain gauges at every 30° were used for the specimens with the diameter of 200 mm. It is worth noting that there were three strain gauges located in the overlapping zone for CFRP jacket wrapped ECC specimens. Four strain gauges with the gauge length of 20 mm were installed in the mid-height of the column in the axial direction at every 90° to measure the axial strains. Meanwhile, four LVDTs were put between the top and bottom loading plates to measure the axial shortening behavior of the specimen. Axial load, strain gauge readings and LVDT readings were recorded by a data logger simultaneously.

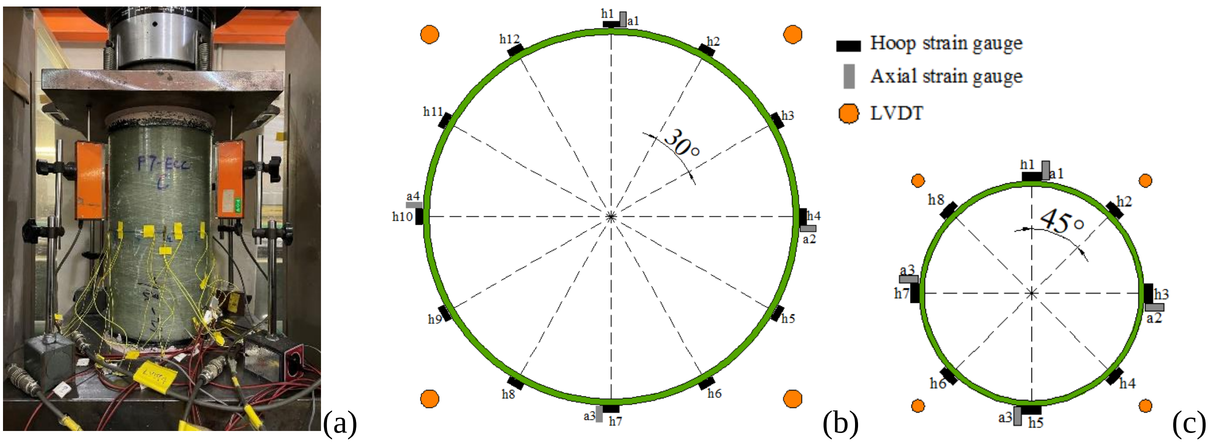

Fig. 3. Test setup and instrumentations: (a) test setup; (b) instrumentation for specimen with diameter of 200 mm; (c) instrumentation for specimen with diameter of 100 mm

Displacement-controlled loading method, with the displacement loading rate of 0.24 mm/min, was adopted for the axial compression tests. Axial load was applied until FRP rupture for the specimens subjected to monotonic compression. For cyclic compression tests, the specimen was loaded to the first target unloading displacement, then unloaded to the load level which was approximately 0 kN, followed by the reloading process until reaching the second target unloading displacement that was larger than the first one. The unloading/reloading processes were repeated until the specimen failure. The first target unloading displacement and the difference of the target unloading displacements in the next and the previous loading cycles were nearly kept constant. They were both approximately 4 mm for 100 mm × 200 mm specimens and 2 mm for 200 mm × 400 mm specimens. This unloading/reloading procedure was automatically controlled by a preset program.

3. Test results and discussions

3.1 Failure modes

Failure modes for the tested specimens are shown in Fig. 4. For plain ECC cylinders, inclined and vertical dominated cracks can be observed as shown in Fig. 4(a), which lead to shear and splitting failure of ECC under compression. Meanwhile, multiple microcracks near the major cracks as well as the fibers bridging through the cracks could be observed. All the FRP-confined ECC specimens failed by FRP rupture in the hoop direction as shown in Fig. 4(b). For specimens with GFRP tubes, white patches were observed firstly during the loading process, which indicated that resin failure occurred. With further axial shortening, GFRP tube rupture occurred at one location and then propagated along the column within the whole height region. For CFRP jacket confined ECC specimens, FRP ruptured at one location and peeled off within the same height region. When GFRP tube or CFRP jacket was removed, the inner cracking pattens of confined ECC can be observed as shown in Fig. 4(c). Multiple fine cracks were distributed around the column in a relatively uniform manner. There were no localized large cracks and failure could be observed. The failure phenomenon and pattern of specimens under cyclic loading are similar to those of specimens under monotonic loading, which can be observed in Figs. 4(b) and (c).

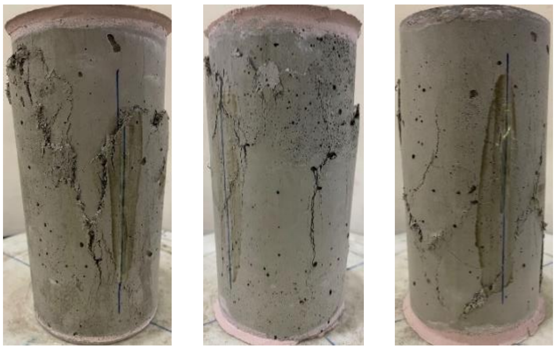

(a) Failure of plain ECC cylinder

(b) FRP rupture

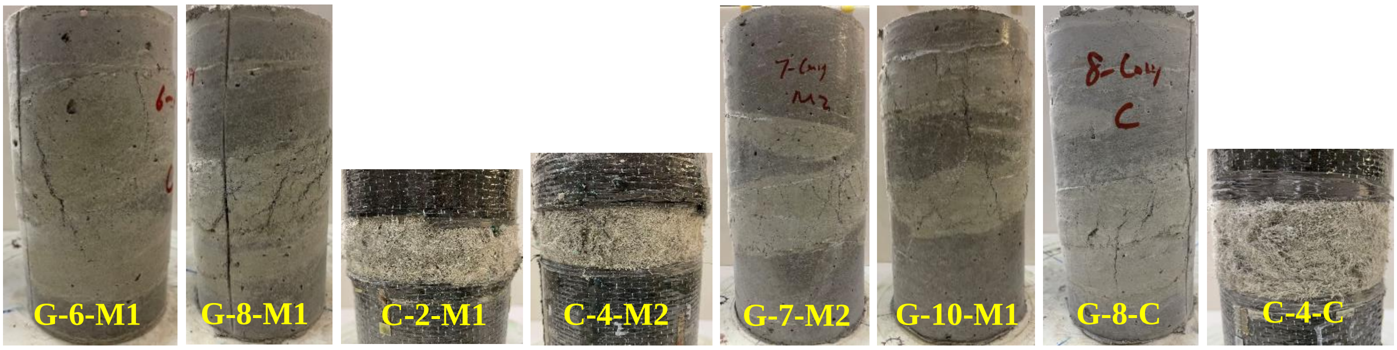

(c) Cracking of confined ECC

Fig. 4 Failure modes of tested specimens

3.2 Axial stress-axial strain responses

Axial stress-axial strain curves for the tested FRP-confined ECC specimens are plotted in Fig. 5. It is worth noting that the axial strain can be determined by both the axial strain gauges and the full height LVDTs. The readings of the four axial strain gauges were nearly the same at the elastic stage before ECC cracking, indicating the pure axial compression applied on the specimen without eccentricity. However, with the increase of loading, the readings of the four strain gauges deviated with each other. This behavior is also reported in the literature [35] and is believed to be caused by the non-uniform damage and cracking of inner concrete. Strain gauges would also be damaged in the later loading stage because of the relatively large axial deformation. On the other hand, the readings of the four LVDTs, which represented the axial shortening of the specimen, were almost the same during the whole loading process. Meanwhile, axial strain calculated by the LVDTs were close to that recorded by the strain gauges at the elastic stage. Therefore, axial strain is determined with the average reading of the four LVDTs and the corresponding specimen height in this study for analysis and discussions.

FRP-confined ECC exhibits a similar typical stress-strain response as FRP-confined normal concrete, in terms of the curve shape. The monotonic stress-strain curve consists of two approximately linear portions connected by a smooth transition zone [36]. Under cyclic loading, axial stress decreases more and more slowly with the decrease of axial strain in the unloading curve till the reloading point where the stress is zero [37,38]. For the reloading curve, a linear portion followed by the nonlinear portion till the next unloading point can be observed [37,38]. Strain hardening behavior can be observed for all the specimens, which indicates the effective confinement provided by FRP and enhanced compressive strength and strain that have achieved. Test curves for two identical specimens under axial monotonic compression (M1 and M2) nearly coincide with each other as shown in Fig. 5, demonstrating the repeatability of the test results. The envelope curves for the specimens under cyclic compression are close to the stress-strain curves for those under monotonic compression as shown in Fig. 5.

In previous studies, it was found that the ultimate compressive strength and strain of specimens under cyclic compression could be larger than those of specimens under monotonic compression, for both FRP-confined normal concrete [37,38] and FRP-confined ECC [24]. This behavior is observed for G-6 specimens in this current study, as shown in Fig. 5(a). For other specimens, it can be found that the cyclically loaded specimens can generally develop the slightly larger ultimate axial strain and the similar ultimate compressive strength in comparison to the counterpart monotonically loaded specimens, as shown in Figs. 5(b-f). It can also be observed in Fig. 5 that with the increase of FRP thickness for specimens with the same diameter and FRP material (i.e. comparing Figs. 5(a) and (b) for specimens with the diameter of 100 mm and 6 or 8 layers of GFRP tube; Figs. 5(c) and (d) for specimens with the diameter of 200 mm and 7 or 10 layers of GFRP tube; Figs. 5(e) and (f) for specimens with the diameter of 100 mm and 2 or 4 layers of CFRP jacket), the ultimate compressive strength and ultimate axial strain were increased accordingly due to the larger confining stiffness. In terms of the two confinement materials used, i.e. GFRP tube and CFRP jacket, the stress-strain responses are similar and there is no obvious difference observed.

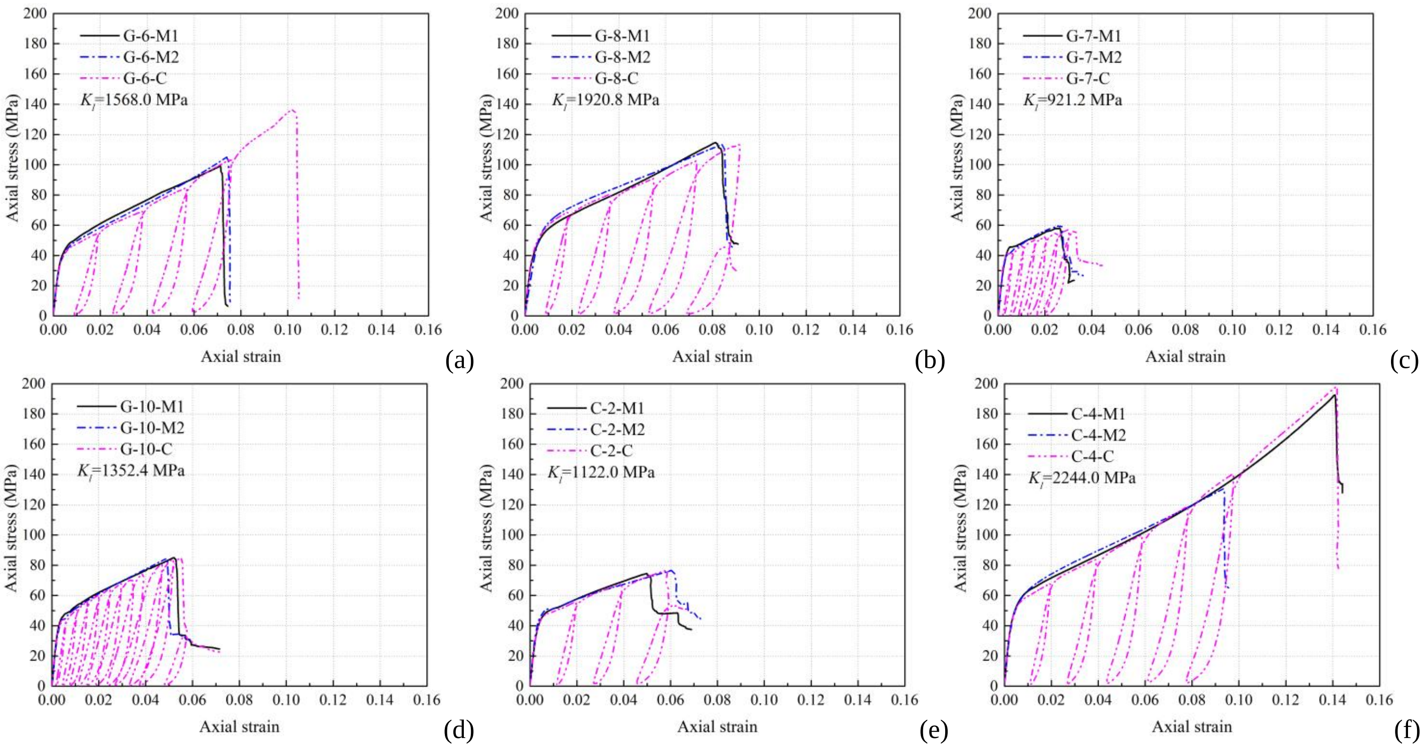

Fig. 5 Axial stress-axial strain curves for FRP-confined ECC specimens

3.3 Hoop strain-axial strain responses

Dilation behavior is of vital importance for analysis of confinement effect of FRP-confined concrete. Hoop strain-axial strain curves for the tested specimens are plotted in Fig. 6, representing the dilation behavior of FRP-confined ECC. Tensile hoop strain is assigned with negative value, while compressive axial strain is assigned with positive value. For GFRP tube confined ECC specimens, hoop strain is averaged from readings of all the eight or twelve hoop strain gauges. For CFRP jacket confined ECC, hoop strain is averaged from the readings of the five strain gauges outside the overlapping zone. It is noted that the hoop strain gauges may be damaged due to the large axial deformation of GFRP tube or CFRP jacket and cannot hold on to the FRP rupture. In Fig. 6, the hoop strain-axial strain curve was linearly extended to the point corresponding to ultimate axial strain at FRP rupture. Hoop rupture strains $\varepsilon_{h,rup}$ for the tested FRP-confined ECC specimens are summarized in Table 4. Similar to axial stress-axial strain responses, the envelope curve for the specimen under cyclic loading is close to the curves for the counterpart specimens under monotonic loading as presented in Fig. 6. With the increase of FRP thickness for specimens with the same diameter and FRP material (i.e. comparing Figs. 6(a) and (b) for specimens with the diameter of 100 mm and 6 or 8 layers of GFRP tube; Figs. 6(c) and (d) for specimens with the diameter of 200 mm and 7 or 10 layers of GFRP tube; Figs. 6(e) and (f) for specimens with the diameter of 100 mm and 2 or 4 layers of CFRP jacket), hoop strain develops more slowly because of the stronger confinement. The ultimate axial strain will also be further improved accordingly.

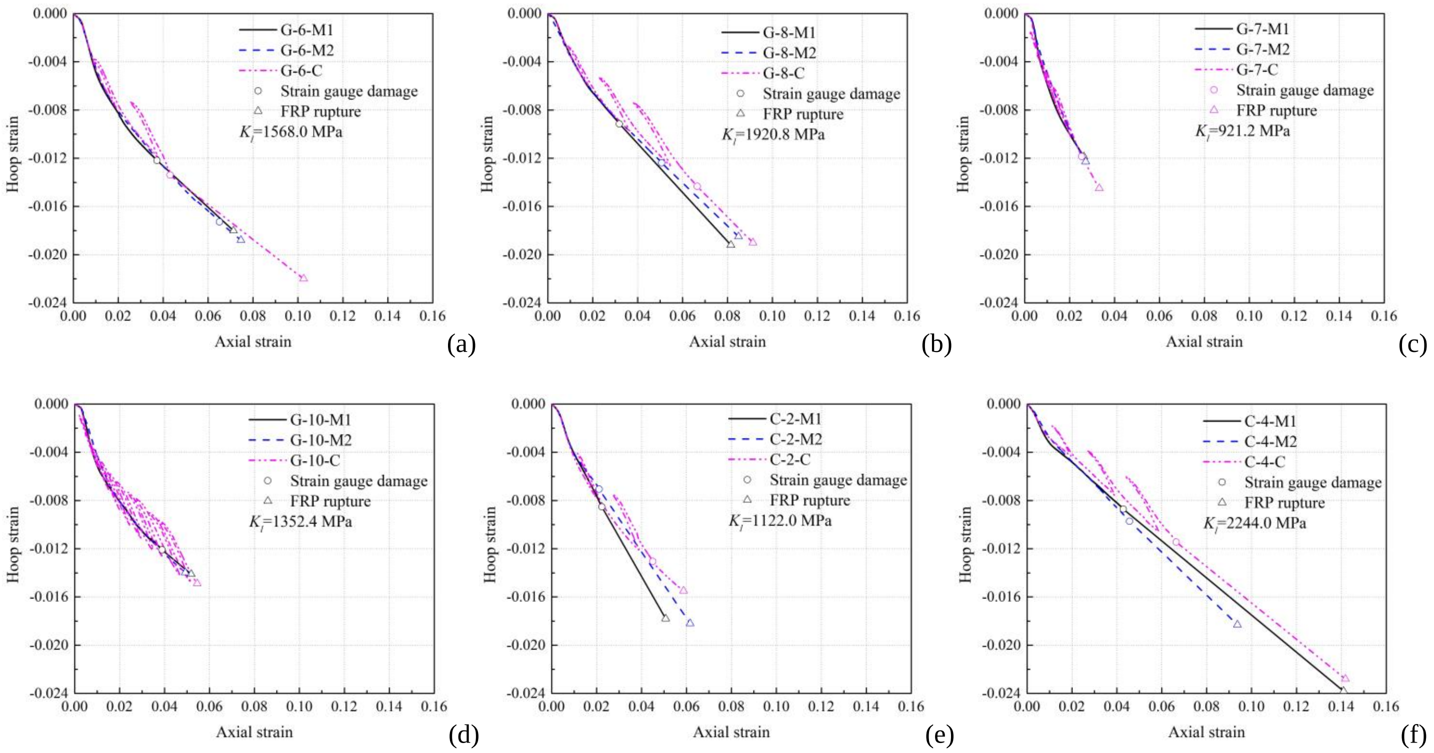

Fig. 6 Hoop strain-axial strain curves for FRP-confined ECC specimens

3.4 Hoop strain distributions

Hoop strain distribution and cracking behavior of confined ECC are presented together in Fig. 7 for the tested specimens. The hoop strain distributions were plotted based on the readings of the strain gauges attached in the hoop direction in the mid-height of the column. Due to the fiber bridging effect in ECC material, multiple fine cracks, instead of localized cracks, are able to be developed for FRP-confined ECC. Based on the hoop strain plots, it can be observed that the specimens under cyclic compression can generally develop more uniform hoop strain distributions in comparison to counterpart specimens under monotonic compression. For CFRP jacket wrapped ECC specimens (C-2 specimens and C-4 specimens), strain values at locations h6, h7 and h8, which are in the overlapping zone, are lower than those at the other locations. Hoop strains at these three locations are excluded when determining the average hoop strains of the FRP-confined ECC specimens.

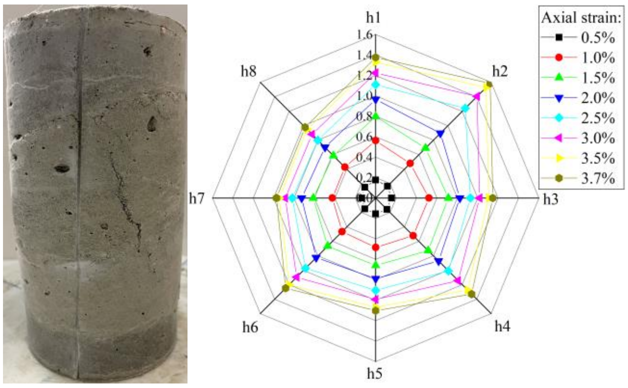

G-6-M1

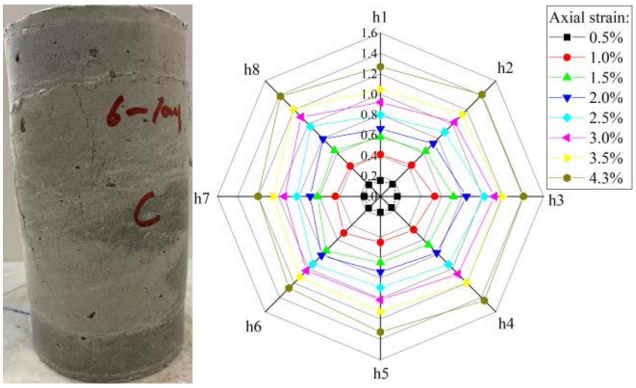

G-6-C

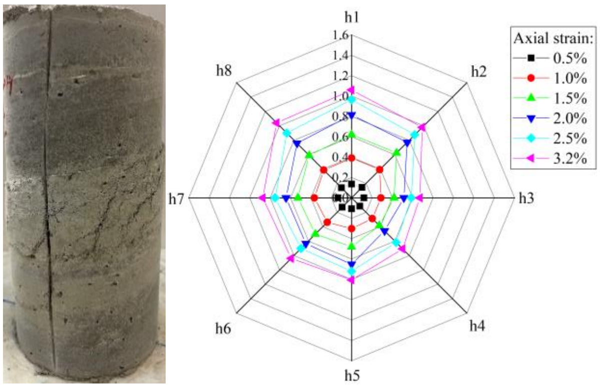

G-8-M1

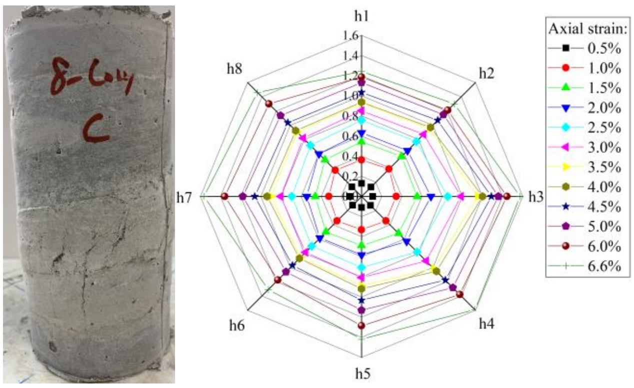

G-8-C

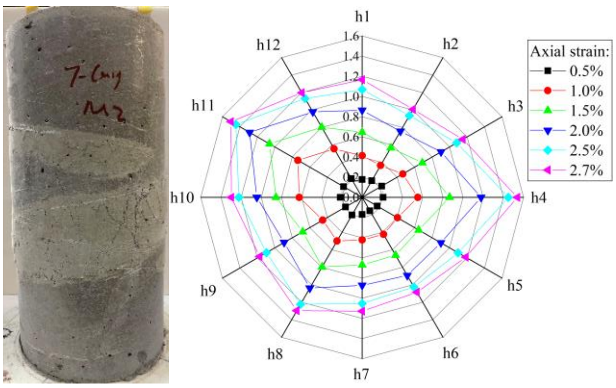

G-7-M2

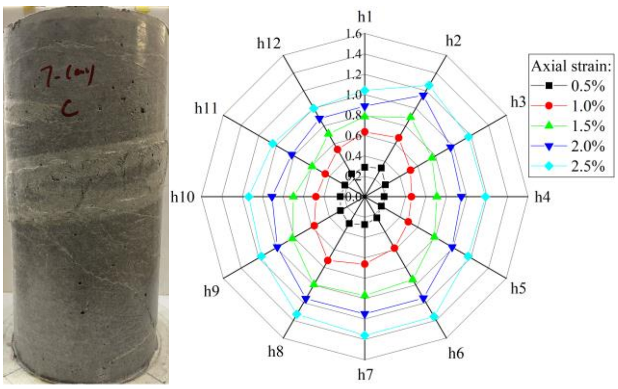

G-7-C

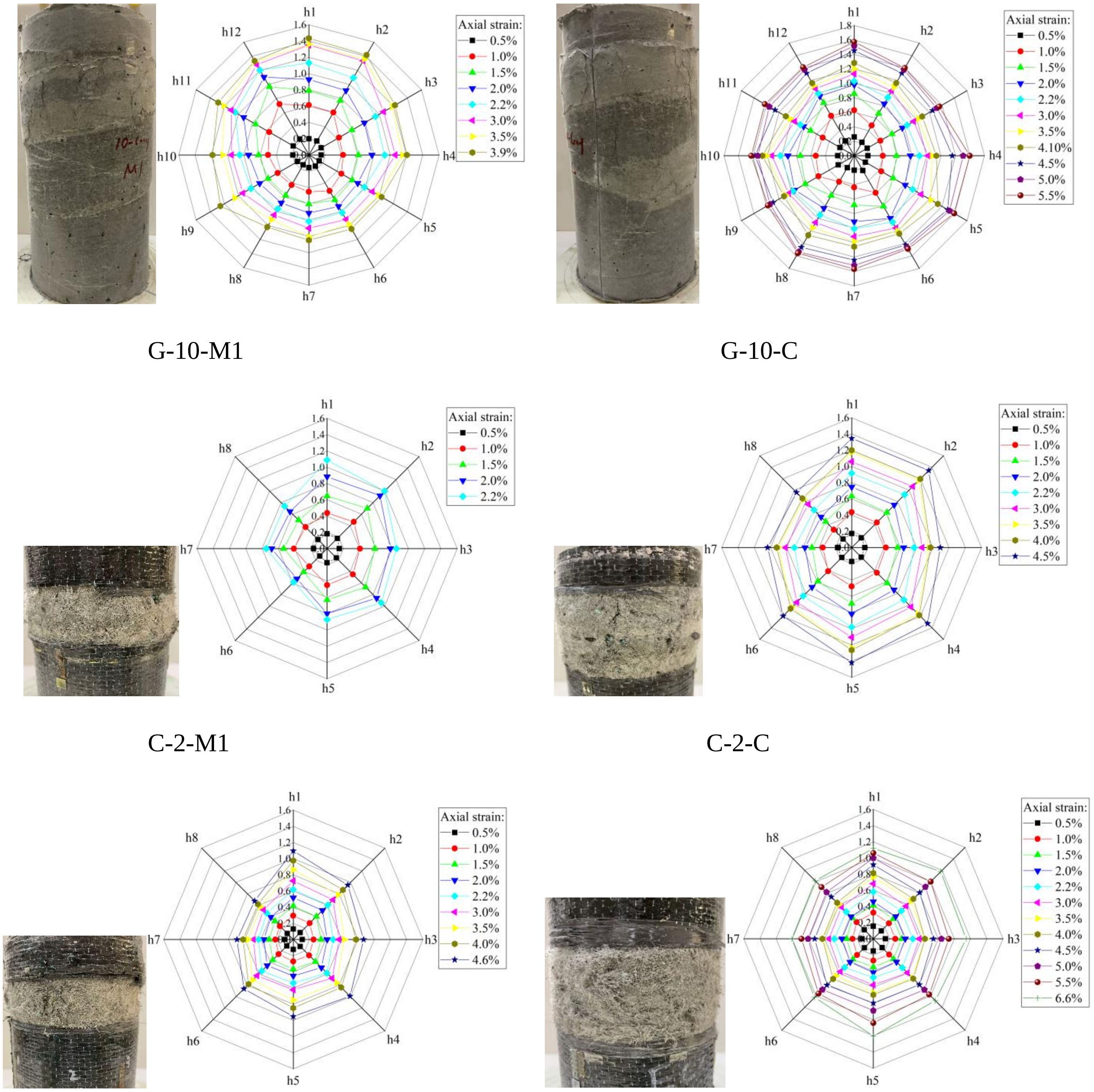

G-10-M1 G-10-C

C-2-M1 C-2-C

C-4-M2 C-4-C

Fig. 7 Hoop strain distribution behavior and cracking behavior for the tested specimens under monotonic and cyclic loadings

3.5 Ultimate conditions

Ultimate conditions corresponding to FRP rupture, including the ultimate compressive strength f'_{cu} and ultimate axial strain ε_{cu} as summarized for each tested specimen in Table 4, are discussed in this section. Confinement level is closely related to the ultimate conditions for FRP-confined concrete. Actual confining pressure $f_{lu,a}$ corresponding to FRP rupture can be determined as follows:

$$f_{lu,a} = K_l \varepsilon_{h,rup} = \frac{2E_f t_f \varepsilon_{h,rup}}{D} \tag{1}$$

in which E_f and t_f are elastic modulus and thickness of confining FRP; D is the diameter of confined ECC; $\varepsilon_{h,rup}$ is the actual hoop rupture strain of FRP; K_l is the confining stiffness. Fig. 8 presents the relations between strength enhancement ratio f'_{cu}/f'_{c0} as well as strain enhancement ratio $\varepsilon_{cu}/\varepsilon_{c0}$ and actual confinement ratio $f_{lu,a}/f'_{c0}$. It can be seen that both the strength and strain enhancement ratios increase with the increase of confinement ratio.

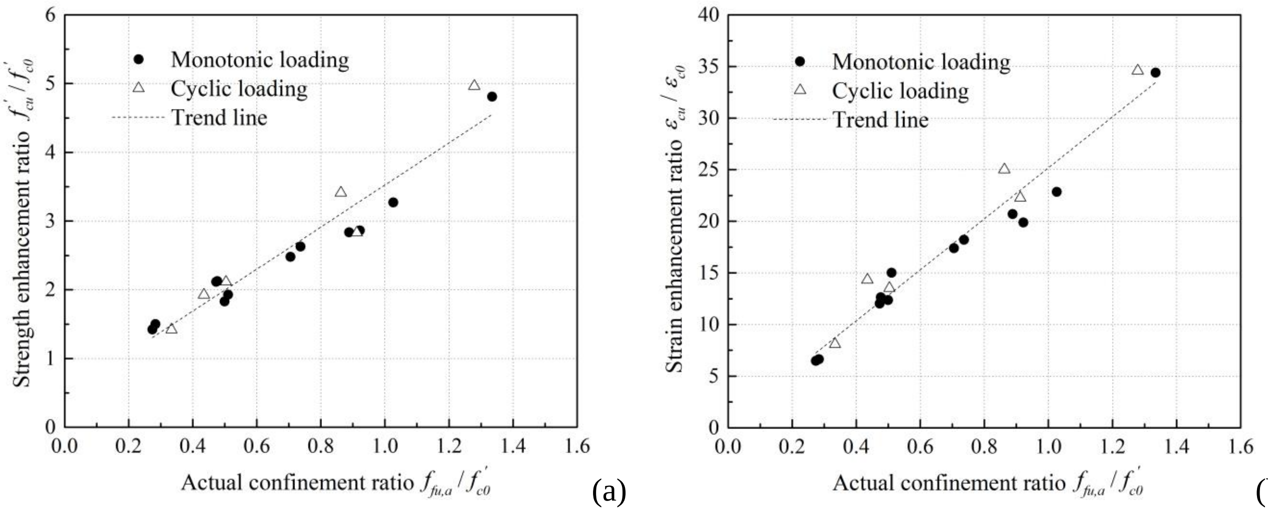

(a) (b)

Fig. 8 Relations between strength/strain enhancement ratio and actual confinement ratio

Lam and Teng [36] proposed the design equations for predicting the ultimate compressive strength and ultimate axial strain based on a database of normal strength concrete confined by different types of FRP with the following expressions:

$$\frac{f'_{cu}}{f'_{c0}} = 1 + k_1 \frac{f_{lu,a}}{f'_{c0}} \tag{2}$$

$$\frac{\varepsilon_{cu}}{\varepsilon_{c0}} = c + k_2 \frac{f_{lu,a}}{f'_{c0}} \tag{3}$$

in which k_1 and k_2 can be regarded as strength and strain enhancement coefficients and c is constant. Teng et al. [39] developed the refined version of the equations later on with a more versatile database. These prediction equations have been widely accepted and adopted by design specifications [40,41]. Dang et al. [24] proposed the design expressions to predict the ultimate compressive strength and ultimate axial strain based on self-conducted test results of FRP-confined ECC. The formula forms are similar to those proposed by Lam and Teng [36] and Teng et al. [39], but with different coefficients. These existing equations are evaluated in this section. Comparisons between the test results and prediction results by these equations are summarized in Tables 5 and 6 and Fig. 9. It can be observed that both Lam and Teng’s model [36] and Teng et al.’s model [39] significantly overestimate the ultimate compressive strength, while Teng et al.’s model [39] underestimates the ultimate axial strain to a large extent. It demonstrates that the equations proposed based on FRP-confined normal concrete may not be applicable to FRP-confined ECC. By contrast, Dang et al.’s model [24], developed by a limited test database of FRP-confined

ECC, could provide much better predictions on the ultimate compressive strength. However, the ultimate axial strain is largely underestimated by Dang et al.'s model [24].

Linear relationship has been considered in the above equations between the actual confining pressure at FRP rupture $f_{lu,a}$ and the strength enhancement f'_{cu}/f'_{c0} or strain enhancement $\varepsilon_{cu}/\varepsilon_{c0}$. It is also found by other studies that non-linear relationship can be used to achieve better prediction results [42,43]. Therefore, power functions relating the actual confining pressure with the strength enhancement ratio or strain enhancement ratio are adopted in this study for the ultimate compressive strength and ultimate axial strain prediction equations for FRP-confined ECC to best fit the test results. The following expressions are proposed through regressions with the obtained test results:

$$\frac{f'_{cu}}{f'_{c0}} = 1 + 2.5\left(\frac{f_{lu,a}}{f'_{c0}}\right)^{1.43} \tag{4}$$

$$\frac{\varepsilon_{cu}}{\varepsilon_{c0}} = 1 + 24\left(\frac{f_{lu,a}}{f'_{c0}}\right)^{1.04} \tag{5}$$

It should be noted that for normal strength concrete without confinement, 0.002 is generally taken as the axial strain at the peak stress, while 0.0035 is generally accepted as the ultimate axial strain [44]. It yields that the ultimate axial strain is 1.75 times that of the axial strain at the peak stress. Hence, the constant c is adopted as 1.75 in the original ultimate axial strain prediction equation [36]. It is also worth noting that the constant 1.75 may be adjusted to suit different values for the strain at the peak stress of unconfined concrete and the ultimate axial strain of unconfined concrete in a specific case [39]. Cui and Sheikh [42] and Liao et al. [43] adopted the constant $c = 1$ in the ultimate axial strain prediction equations for FRP-confined high strength concrete (HSC) and FRP-confined ultra-high performance concrete (UHPC), considering that the strain at the peak stress of unconfined concrete is the same as the ultimate compressive strain of unconfined concrete. Similarly, the compressive behavior of unconfined ECC (as shown in Fig. 1) is different from that of unconfined normal concrete. There is a sudden drop at the peak stress, followed by the residual stress decreasing gradually until a relatively large axial strain. It is hard to define the ultimate axial strain. Therefore, the constant $c = 1$ is conservatively adopted in Eq. (5), considering that the ultimate axial strain is the same as the axial strain at the peak stress for unconfined ECC. Comparisons between the test results and predicted results by the newly proposed equations are presented in Tables 5 and 6 and Fig. 9. The close agreements show that the proposed equations could provide good predictions on the ultimate compressive strength and ultimate axial strain for the tested FRP-confined ECC specimens. It is worth noting the equations are only developed and validated with the test results obtained in this study. More data may be needed to further verify their performance in a broader range.

Table 5 Predictions of design equations on ultimate compressive strength

Specimen label	Test results	Predictions by Lam and Teng [36]		Predictions by Teng et al. [39]		Predictions by Dang et al. [24]		Predictions by the proposed Eq. (4)	
	$f'_{cu,test}$ (MPa)	$f'_{cu,pred}$ (MPa)	$\frac{f'_{cu,test}}{f'_{cu,pred}}$	$f'_{cu,pred}$ (MPa)	$\frac{f'_{cu,test}}{f'_{cu,pred}}$	$f'_{cu,pred}$ (MPa)	$\frac{f'_{cu,test}}{f'_{cu,pred}}$	$f'_{cu,pred}$ (MPa)	$\frac{f'_{cu,test}}{f'_{cu,pred}}$
G-6-M1	99.2	133.1	0.75	132.6	0.75	110.6	0.90	100.7	0.98
G-6-M2	105.2	137.3	0.77	136.8	0.77	113.7	0.93	104.6	1.01
G-6-C	136.5	153.8	0.89	153.2	0.89	126.2	1.08	120.9	1.13
G-8-M1	114.6	161.7	0.71	162.5	0.71	132.2	0.87	129.0	0.89
G-8-M2	113.5	156.3	0.72	158.1	0.72	128.8	0.88	124.4	0.91
G-8-C	113.3	160.4	0.71	161.2	0.70	131.2	0.86	127.7	0.89
G-7-M1	56.9	76.2	0.75	74.3	0.77	67.4	0.84	55.7	1.02
G-7-M2	60.0	77.4	0.78	75.5	0.80	68.3	0.88	56.5	1.06
G-7-C	56.8	84.1	0.68	81.8	0.69	73.4	0.77	60.8	0.93
G-10-M1	85.0	102.9	0.83	101.9	0.83	87.7	0.97	74.7	1.14
G-10-M2	84.6	102.5	0.83	101.5	0.83	87.3	0.97	74.3	1.14
G-10-C	84.6	106.5	0.79	105.4	0.80	90.4	0.94	77.5	1.09
C-2-M1	73.2	105.9	0.69	103.8	0.71	89.9	0.81	77.0	0.95
C-2-M2	77.1	107.4	0.72	105.3	0.73	91.1	0.85	78.2	0.99
C-2-C	77.0	97.4	0.79	95.6	0.81	83.5	0.92	70.4	1.09
C-4-M1	192.4	216.2	0.89	218.8	0.88	173.5	1.11	191.2	1.01
C-4-M2	130.8	175.5	0.75	177.5	0.74	142.7	0.92	143.8	0.91
C-4-C	198.5	208.8	0.95	211.3	0.94	167.9	1.18	182.2	1.09
Mean			0.78		0.78		0.93		1.01
CoV			0.095		0.090		0.110		0.084

Table 6 Predictions of design equations on ultimate axial strain

Specimen label	Test results	Predictions by Lam and Teng [36]		Predictions by Teng et al. [39]		Predictions by Dang et al. [24]		Predictions by the proposed Eq. (5)	
	$\varepsilon_{cu,test}$	$\varepsilon_{cu,pred}$	$\frac{\varepsilon_{cu,test}}{\varepsilon_{cu,pred}}$	$\varepsilon_{cu,pred}$	$\frac{\varepsilon_{cu,test}}{\varepsilon_{cu,pred}}$	$\varepsilon_{cu,pred}$	$\frac{\varepsilon_{cu,test}}{\varepsilon_{cu,pred}}$	$\varepsilon_{cu,pred}$	$\frac{\varepsilon_{cu,test}}{\varepsilon_{cu,pred}}$
G-6-M1	0.0713	0.0747	0.95	0.0599	1.19	0.0529	1.35	0.0726	0.98
G-6-M2	0.0746	0.0791	0.94	0.0634	1.18	0.0549	1.36	0.0757	0.98
G-6-C	0.1025	0.0975	1.05	0.0777	1.32	0.0631	1.63	0.0885	1.16
G-8-M1	0.0815	0.0980	0.83	0.0753	1.08	0.0656	1.24	0.0945	0.86
G-8-M2	0.0849	0.0933	0.91	0.0717	1.18	0.0635	1.34	0.0911	0.93
G-8-C	0.0913	0.0967	0.94	0.0743	1.23	0.0650	1.40	0.0935	0.98
G-7-M1	0.0266	0.0290	0.92	0.0261	1.02	0.0264	1.01	0.0297	0.90
G-7-M2	0.0272	0.0300	0.91	0.0270	1.01	0.0271	1.01	0.0306	0.89
G-7-C	0.0332	0.0362	0.92	0.0324	1.03	0.0306	1.08	0.0355	0.93
G-10-M1	0.0518	0.0481	1.08	0.0401	1.29	0.0387	1.34	0.0496	1.04
G-10-M2	0.0493	0.0476	1.03	0.0397	1.24	0.0384	1.28	0.0493	1.00
G-10-C	0.0555	0.0515	1.08	0.0428	1.30	0.0404	1.37	0.0523	1.06
C-2-M1	0.0507	0.0547	0.93	0.0469	1.08	0.0411	1.24	0.0519	0.98
C-2-M2	0.0616	0.0563	1.09	0.0482	1.28	0.0418	1.47	0.0530	1.16
C-2-C	0.0587	0.0461	1.27	0.0397	1.48	0.0367	1.61	0.0455	1.29
C-4-M1	0.1410	0.1521	0.93	0.1125	1.25	0.0906	1.56	0.1370	1.03
C-4-M2	0.0937	0.1062	0.88	0.0791	1.18	0.0713	1.31	0.1052	0.89

C-4-C	0.1418	0.1434	0.99	0.1062	1.34	0.0871	1.63	0.1312	1.08
Mean			0.98		1.20		1.35		1.01
CoV			0.103		0.102		0.137		0.108

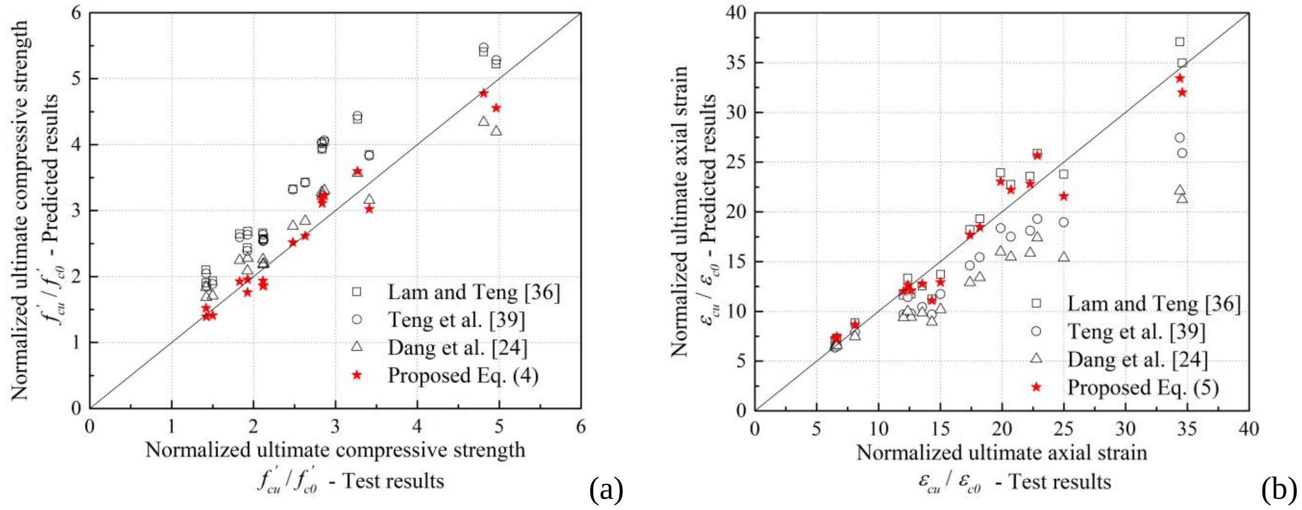

Fig.9 Comparisons of ultimate conditions between test results and design equation predictions

4. Analysis-oriented model

An analysis-oriented model is proposed to describe the overall stress-strain behavior of FRP-confined ECC under monotonic axial compression in this section. Fig. 10 shows the procedures of developing analysis-oriented model for FRP-confined concrete. The relation between axial strain ε_c and hoop strain ε_h (which is also termed as lateral strain ε_l) is plotted in Fig. 10(a), reflecting the dilation behavior of confined concrete. As elastic material, tensile stress of FRP is linearly related to the tensile strain, which equals to the lateral strain ε_l. Confining pressure f_l can then be calculated as the following Eq. (6) and plotted versus lateral strain ε_l as shown in Fig. 10(b).

$$f_l = K_l \varepsilon_l = \frac{2E_f t_f \varepsilon_l}{D} \tag{6}$$

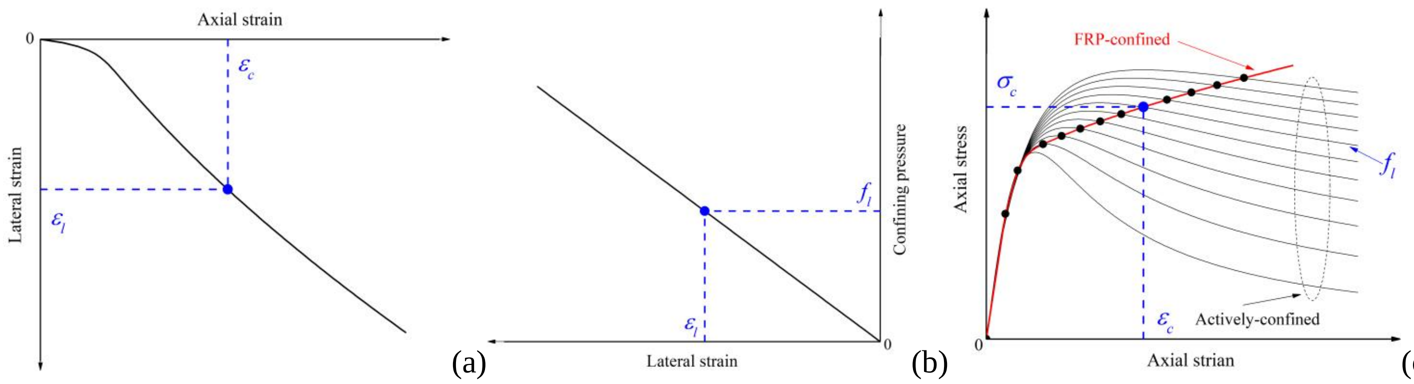

Fig. 10 Generation of the stress-strain curve for FRP-confined concrete: (a) lateral strain-axial strain relation (dilation model); (b) confining pressure-lateral strain relation; (c) Actively-confined and FRP-confined curves.

Fig. 10(c) shows the axial stress-axial strain curves ($\sigma_c - \varepsilon_c$) of actively-confined concrete, in which each curve stands for a specific confining pressure. When an axial strain ε_c is given for FRP-confined concrete, the corresponding lateral strain ε_l can be calculated based on the dilation model (Fig. 10(a)), followed by the determination of confining pressure f_l (Fig. 10(b)). With the axial strain ε_c and confining pressure f_l, the corresponding axial stress σ_c of FRP-confined concrete can be finally determined from the base curves of actively-confined concrete (Fig. 10(c)). The analysis-oriented model for FRP-confined ECC can then be derived and presented following the procedure in this section.

4.1 Database

Research on confined ECC is relatively limited in the literature for the current stage. Test data including both actively-confined and FRP-confined ECC are collected to form the database and adopted to develop the analysis-oriented model for FRP-confined ECC. Li et al. [45] carried out a series of triaxial compression tests on ECC cylinders, with different ECC strengths ranging from 49.5 MPa to 74.4 MPa. These data were used to verify the proposed actively-confined stress-strain model for ECC as presented in section 4.3 of this paper. Dang et al. [24] and Yuan et al. [25] conducted compression tests on ECC confined by GFRP and CFRP jackets, with the ECC strengths of 28.2 MPa, 64.6 MPa and 66.0 MPa. Together with the tests of FRP-confined ECC investigated in this study, this dataset was used to verify the dilation model as presented in section 4.2 of this paper and the proposed analysis-oriented model as presented in section 4.4 of this paper for FRP-confined ECC columns.

4.2 Dilation model

Various dilation models have been developed by different researchers to describe the relationship between lateral strain (hoop strain) and axial strain for FRP-confined normal concrete. Jiang and Teng's model [46] was widely accepted and considered to be applicable to predict the dilation property of both FRP-confined and actively-confined concrete. Lim and Ozbakkaloglu's model [47] and Lai et al.'s model [48] were developed with large database and showed satisfying performance for confined normal concrete ranging from low to high compressive strength. Yuan et al. [25] noted that the dilation behavior of FRP-confined ECC is different from that of FRP-confined normal concrete and proposed the first dilation model targeted for FRP-confined ECC as follows:

$$\frac{\varepsilon_c}{\varepsilon_{c0}} = (1 + 8\frac{f_l}{f'_{c0}})\left[1.015(\frac{-\varepsilon_l}{\varepsilon_{c0}})^{0.305} + 0.221(\frac{-\varepsilon_l}{\varepsilon_{c0}})\right] \tag{7}$$

Performance of the dilation models mentioned above was evaluated as shown in Fig. 11. It can be observed that Jiang and Teng's model [46], Lai et al.'s model [48] and Yuan et al.'s model [25] can provide relatively close results in general, while Lim and Ozbakkaloglu's model [47] gives a larger lateral strain prediction under the same axial strain. When compared with test results, Yuan et al.'s model [25], as expressed in Eq. (7), presents the closest predictions among the four models in terms of the overall lateral strain-axial strain curve. It is expected since Yuan et al.'s model [25] was proposed based on the test data of FRP-confined ECC [25], while the other models were developed based on the test data of FRP-confined normal concrete. However, it is worth noting that for the test data collected from Dang et al. [24], the prediction curves exhibit relatively larger deviations from the test curves as shown in Figs. 11(l-o).

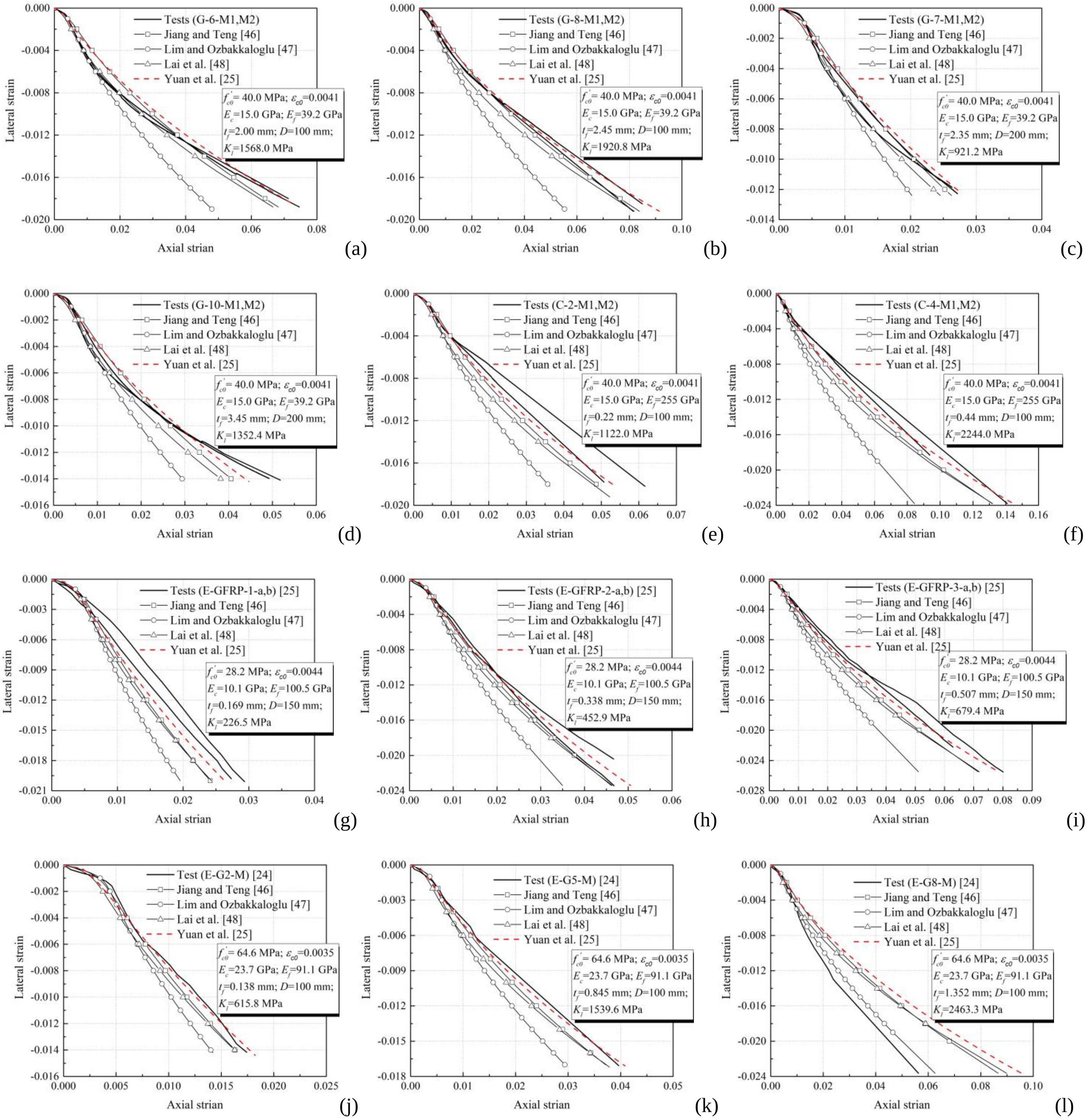

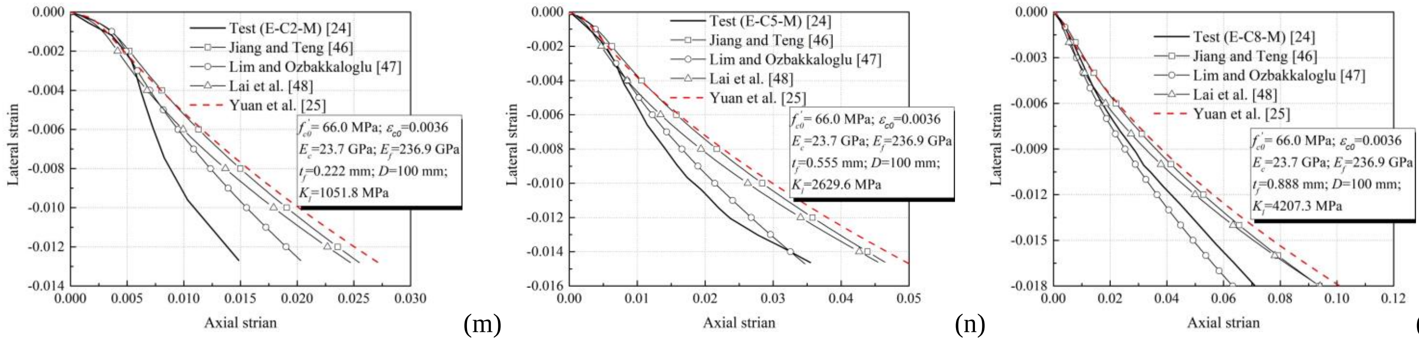

(m) (n) (o)

Fig. 11 Predictions on lateral strain-axial strain curves by different dilation models

The test curves with different confining stiffnesses K_l collected from [24] are plotted in Fig. 12(a) for comparison. It is accepted that for FRP-confined concrete, the larger the confining stiffness is, the lower slope of the lateral strain-axial strain curve should be. It can be noticed that some test curves shown in Fig. 12(a) are not following the trend. For example, the specimen with a larger confining stiffness (E-G8-M with K_l=2463.3 MPa) develops a larger slope of the lateral strain-axial strain curve than the specimen with a lower confining stiffness (E-G5-M with K_l=1539.6 MPa). This group of test data may require further examinations.

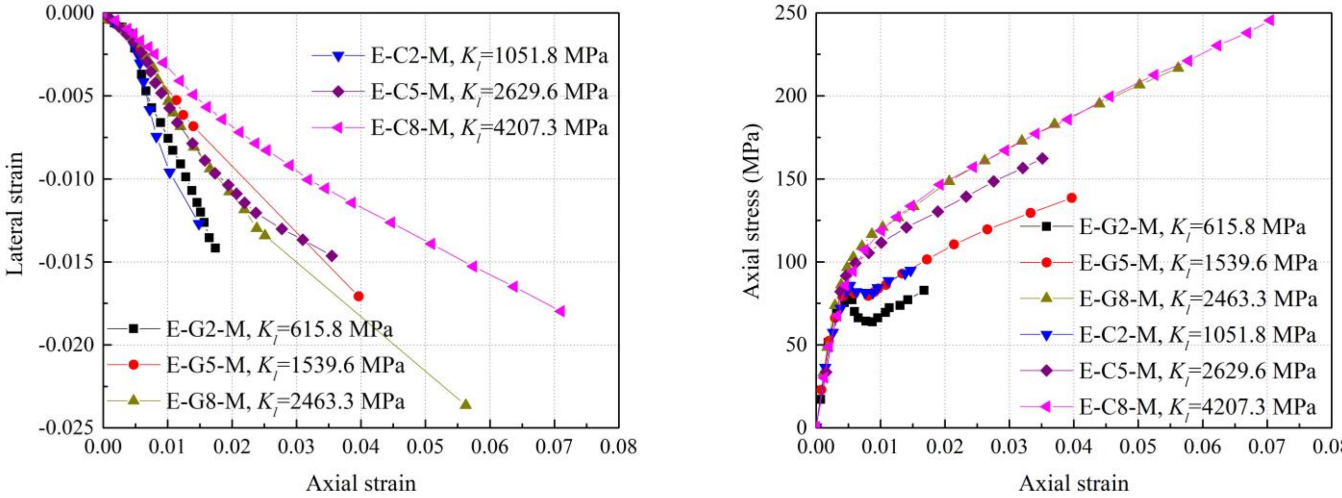

(a) Lateral strain-axial strain curves (b) Axial stress-axial strain curves

Fig. 12 Test data collected from Dang et al. [24]

Comparisons of ultimate axial strain between test results and predicted results by different dilation models are presented in Table 7 and Fig. 13. Yuan et al.'s model [25] could provide the closet predictions as well, with the mean value of 0.97 and CoV value of 0.167 for all the collected data. If the data collected in [24] is excluded, the mean value is 1.02 and the CoV value is 0.077. Therefore, Yuan et al.'s model [25] will be used as the dilation model in the proposed analysis-oriented model for FRP-confined ECC to generate the lateral strain-axial strain relation.

Table 7 Predictions on ultimate axial strain by different dilation models

Data source	Specimen label	Test results	Predictions by Jiang and Teng [46]		Predictions by Lim and Ozbakkaloglu [47]		Predictions by Lai et al. [48]		Predictions by Yuan et al. [25]	
		$\varepsilon_{cu,test}$	$\varepsilon_{cu,pred}$	$\frac{\varepsilon_{cu,test}}{\varepsilon_{cu,pred}}$	$\varepsilon_{cu,pred}$	$\frac{\varepsilon_{cu,test}}{\varepsilon_{cu,pred}}$	$\varepsilon_{cu,pred}$	$\frac{\varepsilon_{cu,test}}{\varepsilon_{cu,pred}}$	$\varepsilon_{cu,pred}$	$\frac{\varepsilon_{cu,test}}{\varepsilon_{cu,pred}}$
Present study	G-6-M1	0.0713	0.0642	1.11	0.0447	1.60	0.0623	1.14	0.0699	1.02
	G-6-M2	0.0746	0.0682	1.09	0.0473	1.58	0.0666	1.12	0.0743	1.00
	G-8-M1	0.0815	0.0838	0.97	0.0561	1.45	0.0819	1.00	0.0914	0.89
	G-8-M2	0.0849	0.0795	1.07	0.0533	1.59	0.0773	1.10	0.0866	0.98
	G-7-M1	0.0266	0.0250	1.06	0.0193	1.39	0.0233	1.14	0.0268	0.99
	G-7-M2	0.0272	0.0260	1.05	0.0200	1.36	0.0243	1.12	0.0279	0.97
	G-10-M1	0.0518	0.0410	1.26	0.0296	1.75	0.0386	1.34	0.0442	1.17
	G-10-M2	0.0493	0.0406	1.21	0.0294	1.68	0.0382	1.29	0.0438	1.13
	C-2-M1	0.0507	0.0480	1.06	0.0352	1.44	0.0467	1.09	0.0522	0.97
	C-2-M2	0.0616	0.0494	1.25	0.0362	1.70	0.0483	1.28	0.0538	1.14
	C-4-M1	0.1410	0.1318	1.07	0.0843	1.67	0.1320	1.07	0.1446	0.98
	C-4-M2	0.0937	0.0898	1.04	0.0587	1.60	0.0870	1.08	0.0978	0.96
Yuan et al. [25]	E-GFRP-1-a	0.0287	0.0244	1.18	0.0198	1.45	0.0246	1.17	0.0266	1.08
	E-GFRP-1-b	0.0299	0.0252	1.19	0.0104	1.47	0.0255	1.17	0.0275	1.09
	E-GFRP-2-a	0.0479	0.0389	1.23	0.0297	1.61	0.0386	1.24	0.0424	1.13
	E-GFRP-2-b	0.0470	0.0464	1.01	0.0352	1.34	0.0466	1.01	0.0509	0.92
	E-GFRP-3-a	0.0633	0.0597	1.06	0.0431	1.47	0.0593	1.07	0.0653	0.97
	E-GFRP-3-b	0.0818	0.0743	1.10	0.0529	1.55	0.0750	1.09	0.0816	1.00
Dang et al. [24]	E-G2-M	0.0171	0.0168	1.02	0.0144	1.19	0.0168	1.02	0.0182	0.94
	E-G5-M	0.0395	0.0369	1.07	0.0292	1.35	0.0369	1.07	0.0402	0.98
	E-G8-M	0.0561	0.0859	0.65	0.0621	1.90	0.0890	0.63	0.0947	0.59
	E-C2-M	0.0147	0.0250	0.59	0.0201	1.73	0.0242	0.61	0.0266	0.55
	E-C5-M	0.0351	0.0460	0.76	0.0341	1.03	0.045	0.78	0.0491	0.71
	E-C8-M	0.0707	0.0938	0.75	0.0632	1.12	0.094	0.75	0.1010	0.70
	Mean			1.04		1.42		1.06		0.97
	CoV			0.169		0.179		0.176		0.167
	Mean*			1.11		1.54		1.14		1.02
	CoV*			0.075		0.078		0.081		0.077

Note: Results of “Mean” and “CoV” are corresponding to all the collected data, including those from present study, Yuan et al. [25] and Dang et al. [24]. Results of “Mean” and “CoV*” are corresponding to the collected data from present study and Yuan et al. [25].

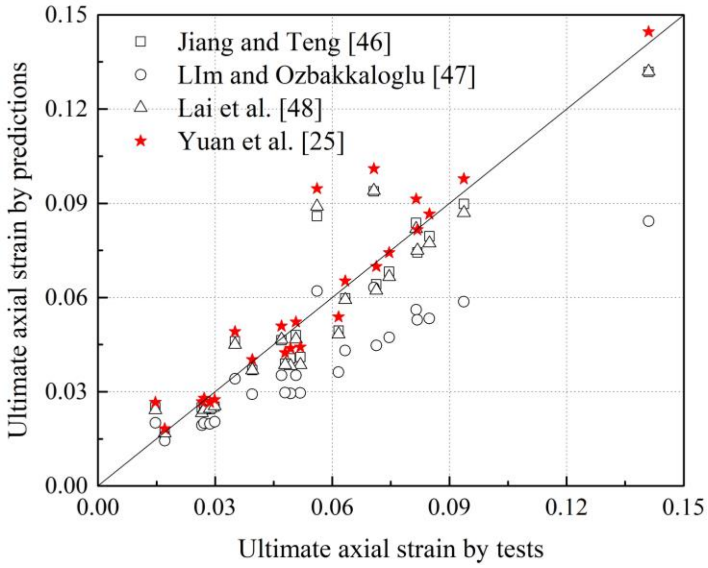

Fig. 13 Comparisons of ultimate axial strain between test results and dilation model predictions

4.3 Actively-confined model

The stress-strain model originally proposed by Popovics [49] is widely accepted and adopted by other researchers for confined concrete. It can be expressed as follows:

$$\sigma_c = \frac{f_{cc}'^{*}(\varepsilon_c/\varepsilon_{cc}^{*})r}{r-1+(\varepsilon_c/\varepsilon_{cc}^{*})^{r}} \tag{8}$$

in which the parameter r is defined as:

$$r = \frac{E_c}{E_c - f_{cc}'^{*}/\varepsilon_{cc}^{*}} \tag{9}$$

where E_c is the elastic modulus of concrete; $f_{cc}'^{*}$ and ε_{cc}^{*} are the peak compressive stress and the corresponding compressive strain of confined concrete under the confining pressure f_l. Various existing actively-confined models adopt the equations of $f_{cc}'^{*}$ and ε_{cc}^{*} that are developed based on confined normal concrete. Due to the different strength and strain enhancement behavior between ECC and normal concrete, these existing actively-confined models may not give the accurate predictions on ECC under active confinement. Li et al. [45] conducted experimental investigations on ECC cylinders with different strengths under various confining pressures and developed the following compressive strength $f_{cc}'^{*}$ and compressive strain ε_{cc}^{*} for ECC under triaxial compression:

$$f_{cc}'^{*} = f_{c0}' + 2.866 f_l \tag{10}$$

$$\varepsilon_{cc}^{*} = \varepsilon_{c0}\left(1 + 7.399\frac{f_l}{f_{c0}'}\right) \tag{11}$$

It can be observed that the strength enhancement ratio of 2.866 and strain enhancement ratio of 7.399 are different from those of 3.5 and 17.5 for actively-confined normal concrete proposed by Jiang and Teng [46].

The axial stress-axial strain curves for ECC under active confinement are collected from Li et al. [45] and plotted in Fig. 14. Axial stress-axial strain curves predicted by the newly proposed actively-confined model, which consists of Eqs. (8-11), are presented in Fig. 14 as well for comparisons with the test results. It is noted that some deviations can be observed in the elastic stage among the test curves representing different confining pressures (as shown in Figs. 14(b-e)). It may be caused by the triaxial compression test deviations. Since the elastic modulus of ECC was not provided in [45], it was determined according to the initial linear stage of the test curve with the confining pressure of 0 MPa. The close agreements demonstrate that the proposed actively-confined model could provide reasonable predictions on the axial stress-axial strain curves for ECC under different levels of active confinement. Therefore, this proposed actively-confined model is adopted as part of the analysis-oriented model for FRP-confined ECC in this study.

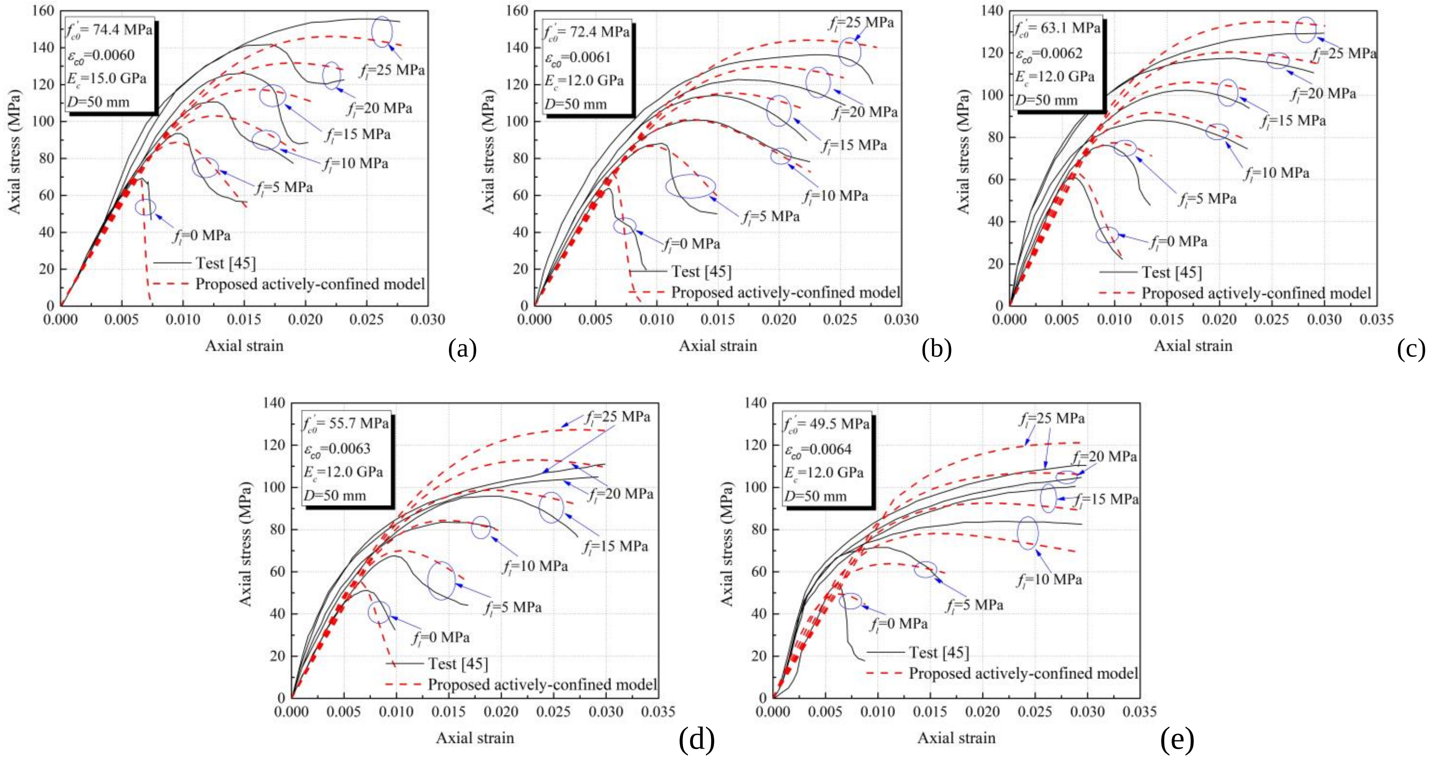

Fig.14 Predictions of proposed actively-confined model

4.4 Proposed analysis-oriented model

With the confining pressure-lateral strain relation as expressed in Eq. (6), the selected dilation model as expressed in Eq. (7) and the proposed actively-confined model as expressed in Eqs. (8-11), the proposed analysis-oriented model for FRP-confine ECC can be generated following the procedures as illustrated in Fig. 10. Fig. 15 shows comparisons of axial stress-axial strain curves between the collected FRP-confined ECC test results and predictions by the proposed model as well as other existing analysis-oriented models. The proposed model is observed to perform obviously better than the other existing models that largely overestimate the axial stress. It is believed to be caused by the reason that the other existing models were developed with the test data of FRP-confined normal concrete, which are not suitable for FRP-confined ECC due to the different characteristics between normal concrete and ECC. Similar to lateral strain-axial strain behavior, it is also noted that the predicted axial stress-strain curves cannot match well with the test curves for the data collected from Dang et al. [24] as shown in Figs. 15(j-o). The test curves with different confining stiffnesses K_l collected from [24] are plotted in Fig. 12(b) for comparison. With the increase of confining stiffness, the slope of the strain hardening stage should also increase accordingly. However, some data presented in Fig. 12(b) are not following this trend. For example, the specimen E-G8-M with K_l=2463.3 MPa develops the larger slope of the strain hardening stage than the specimen E-C5-M with K_l=2629.6 MPa, and the similar slope with the specimen E-C8-M with K_l=4207 MPa.

This group of test data may require further examinations. Comparisons of ultimate compressive strength between test results and predicted results by different analysis-oriented models are presented in Table 8 and Fig. 16. It shows that the proposed analysis-oriented model could provide the best predictions, with the mean value of 1.06 and CoV value of 0.137 for all the collected data. If the data collected in [24] is excluded, the mean value is 1.00 and the CoV value is 0.074.

It is worth noting that path-independence is considered in the generation process of the proposed analysis-oriented model for FRP-confined ECC. It means that axial stress of FRP-confined ECC is considered to be the same as that of actively-confined ECC under the same axial strain and confining pressure. It is believed that this path-independence assumption could be applicable for FRP-confined concrete with normal compressive strength [27,46], while it is not accurate for FRP-confined high strength concrete [47,48,50]. The axial stress of FRP-confined high strength concrete is generally lower than that of actively-confined high strength concrete under the same axial strain and confining pressure, which is termed as path-dependent behavior [48]. In this current study, compressive strength of the investigated ECC is 40.0 MPa. Therefore, it is believed that not much difference would be caused with the adoption of path-independence assumption when generating the analysis-oriented model. The proposed analysis-oriented model for FRP-confined ECC is developed and verified based on the available test data in this current study. Comprehensive examinations with more test data may be needed in future studies. Meanwhile, analysis-oriented models considering path-dependence could also be further developed with more test data of both actively-confined ECC and FRP-confined ECC.

Table 8 Predictions on ultimate compressive strength by different analysis-oriented models

Data source	Specimen label	Test results	Predictions by Jiang and Teng [46]		Predictions by Lim and Ozbakkaloglu [47]		Predictions by Lai et al. [48]		Predictions by the proposed analysis-oriented model	
		$f'_{cu,test}$ (MPa)	$f'_{cu,pred}$ (MPa)	$\frac{f'_{cu,test}}{f'_{cu,pred}}$	$f'_{cu,pred}$ (MPa)	$\frac{f'_{cu,test}}{f'_{cu,pred}}$	$f'_{cu,pred}$ (MPa)	$\frac{f'_{cu,test}}{f'_{cu,pred}}$	$f'_{cu,pred}$ (MPa)	$\frac{f'_{cu,test}}{f'_{cu,pred}}$
Present study	G-6-M1	99.2	138.4	0.72	130.2	0.76	157.3	0.63	100.3	0.99
	G-6-M2	105.2	142.7	0.74	133.4	0.79	162.2	0.65	102.7	1.02
	G-8-M1	114.6	168.6	0.68	152.9	0.75	193.2	0.59	120.9	0.95
	G-8-M2	113.5	164.0	0.69	149.6	0.76	187.9	0.60	118.3	0.96
	G-7-M1	56.9	87.3	0.65	77.2	0.74	85.9	0.66	61.2	0.93
	G-7-M2	60.0	79.6	0.75	78.3	0.77	87.4	0.69	61.9	0.97
	G-10-M1	85.0	106.7	0.80	105.2	0.81	119.8	0.71	80.6	1.05
	G-10-M2	84.6	106.2	0.80	104.8	0.81	119.2	0.71	80.3	1.05
	C-2-M1	73.2	109.5	0.67	106.8	0.69	122.5	0.60	79.4	0.92
	C-2-M2	77.1	111.1	0.69	108.1	0.71	124.2	0.62	80.2	0.96
	C-4-M1	192.4	225.5	0.85	192.8	1.00	259.8	0.74	156.3	1.23
	C-4-M2	130.8	183.4	0.71	164.0	0.80	211.2	0.62	132.5	0.99
	E-GFRP-1-a	31.7	43.3	0.73	40.0	0.78	45.6	0.70	30.3	1.05

Yuan et al. [25]	E-GFRP-1-b	32.5	43.7	0.74	40.5	0.80	46.0	0.71	30.4	1.07
	E-GFRP-2-a	44.0	60.2	0.73	59.6	0.74	66.3	0.66	43.2	1.02
	E-GFRP-2-b	45.0	64.7	0.70	64.5	0.70	71.4	0.63	45.4	0.99
	E-GFRP-3-a	54.8	80.9	0.68	83.9	0.65	91.1	0.60	57.5	0.95
	E-GFRP-3-b	55.4	89.6	0.62	91.6	0.60	101.1	0.55	62.1	0.89
Dang et al. [24]	E-G2-M	83.3	93.2	0.89	76.5	1.09	71.5	1.17	57.4	1.45
	E-G5-M	139.0	154.2	0.90	141.4	0.98	156.4	0.89	100.8	1.38
	E-G8-M	217.1	263.2	0.82	229.7	0.95	218.8	0.99	164.7	1.32
	E-C2-M	95.3	130.4	0.73	119.9	0.79	139.4	0.68	90.3	1.06
	E-C5-M	162.8	197.6	0.82	184.1	0.88	218.6	0.74	136.0	1.20
	E-C8-M	245.4	328.1	0.75	274.1	0.90	367.5	0.67	219.6	1.12
	Mean			0.74		0.80		0.70		1.06
	CoV			0.097		0.139		0.192		0.137
	Mean*			0.72		0.76		0.65		1.00
	CoV*			0.077		0.105		0.078		0.074

Note: Results of "Mean" and "CoV" are corresponding to all the collected data, including those from present study, Yuan et al. [25] and Dang et al. [24]. Results of "Mean" and "CoV*" are corresponding to the collected data from present study and Yuan et al. [25].

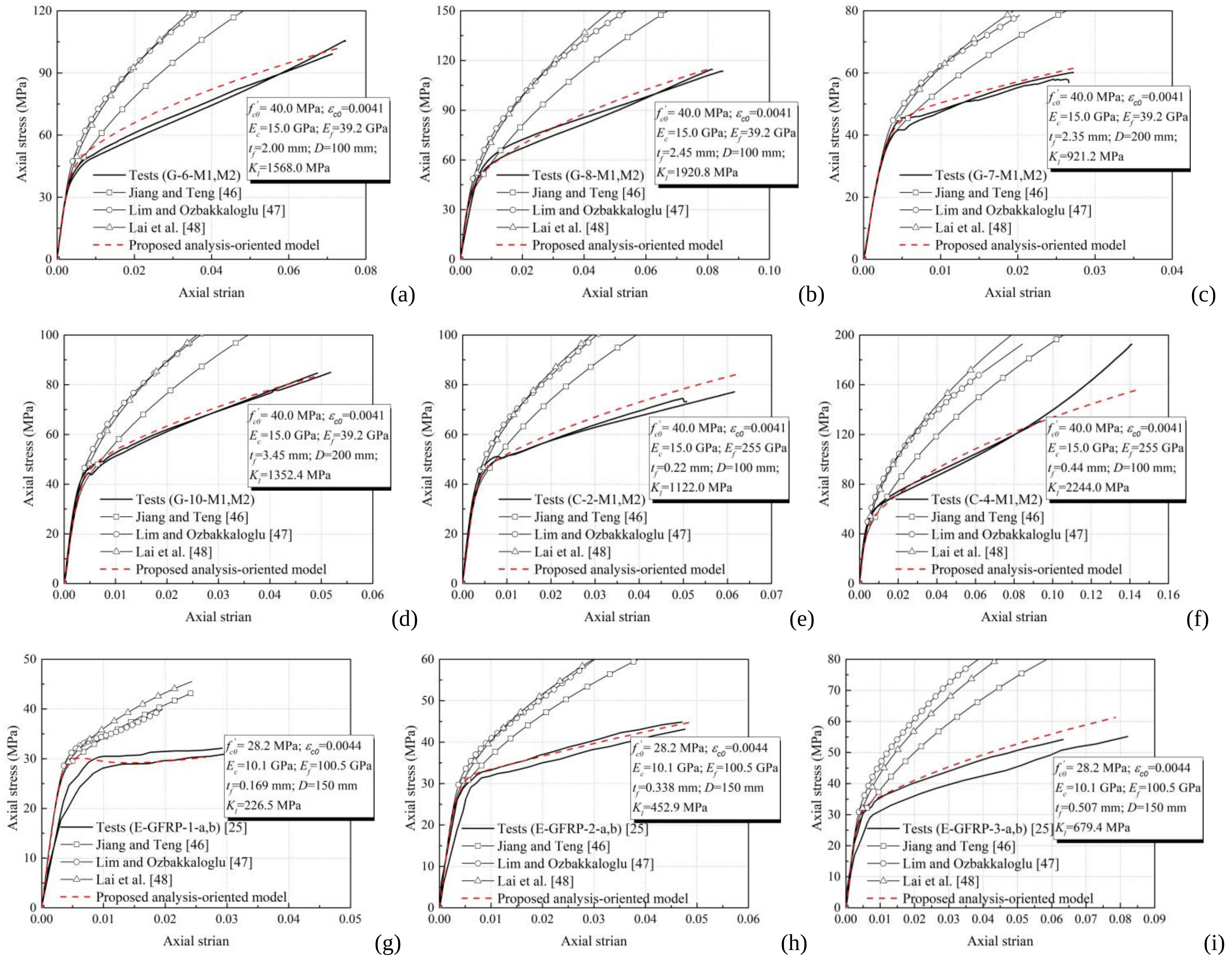

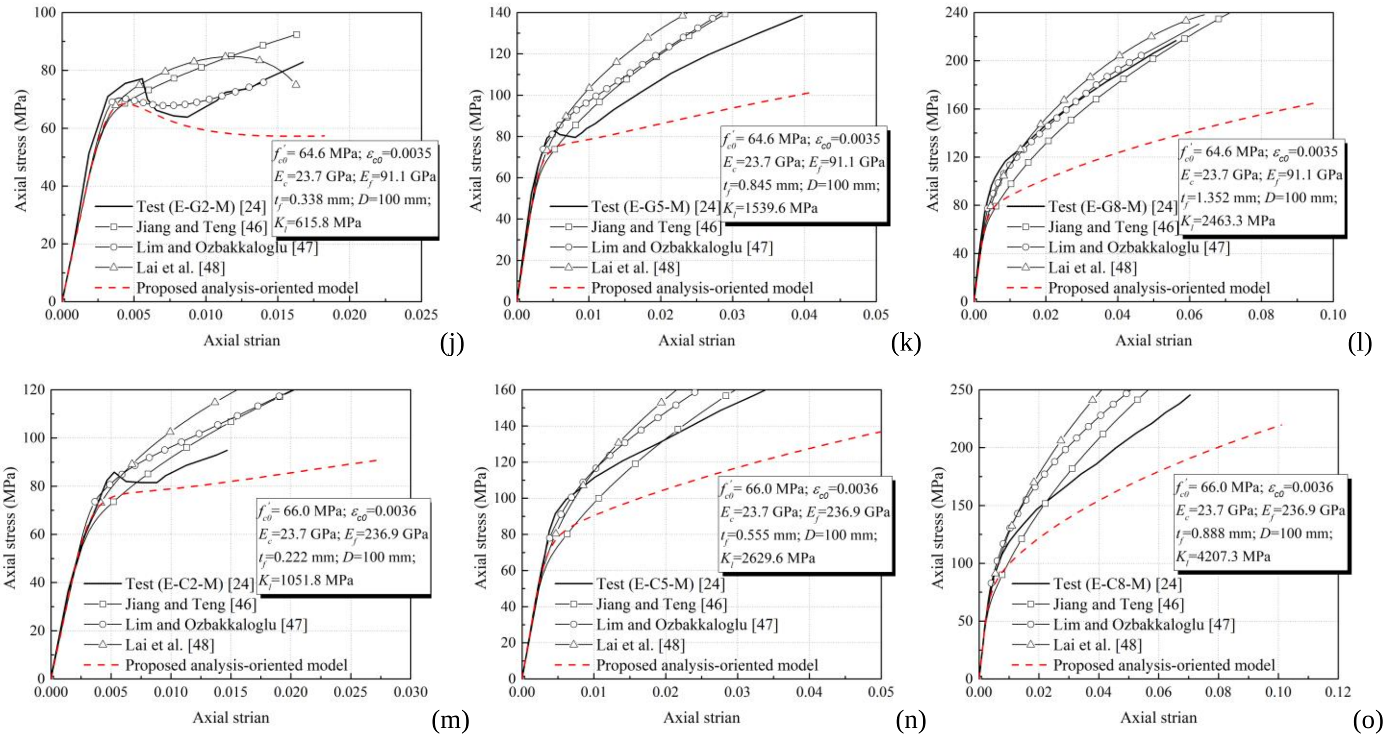

Fig. 15 Predictions on axial stress-axial strain curves by different analysis-oriented models

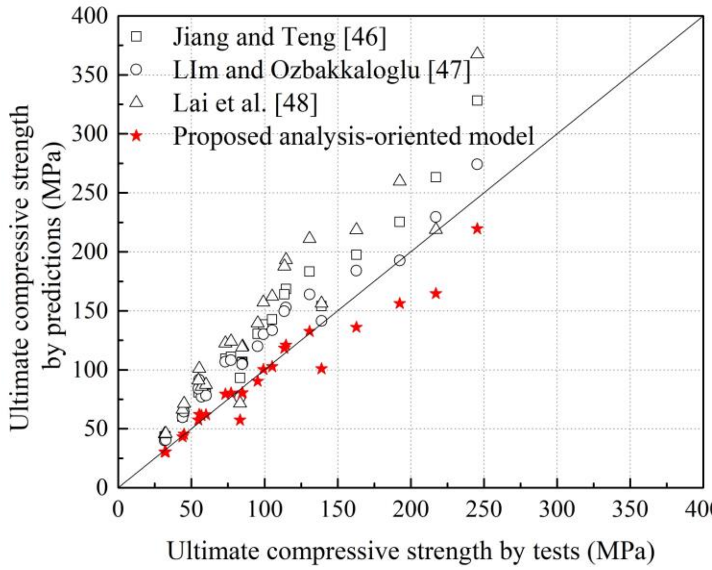

Fig. 16 Comparisons of ultimate compressive strength between test results and analysis-oriented model predictions

5. Conclusions

A total of 18 FRP-confined ECC specimens were tested under axial monotonic and cyclic compression in this study. Failure modes, dilation behavior and stress-strain behavior were presented and analyzed. Design equations were developed to predict the ultimate conditions. Analysis-oriented model was proposed to describe the overall compressive stress-strain behavior of FRP-confined ECC columns. The following conclusions can be drawn within the current scope of this study:

(1) All the FRP-confined ECC columns failed by FRP rupture in the hoop direction. Multiple fine cracks were distributed around the confined ECC in a relatively uniform manner, with no localized large cracks or failure observed.

(2) Strain hardening behavior with a second ascending portion in the stress-strain curve was observed for all the tested specimens. Both the compressive strength and strain of ECC were effectively enhanced with the FRP confinement of different levels. Ultimate axial strains of the tested specimens are relatively large, indicating the good deformability and ductility performance of FRP-confined ECC columns.

(3) Both the stress-strain curve and lateral strain-axial strain curve of the specimens under monotonic compression were close to the corresponding envelope curves of the specimens under cyclic compression. It was observed from the hoop strain plots that the cyclically loaded specimens could generally exbibit the relatively more uniform hoop strain distribution than the counterpart monotonically loaded specimens.

(4) Both the ultimate compressive strength and ultimate axial strain increase with the increase of lateral confining pressure for the tested specimens. Design equations were developed to directly predict the ultimate compressive strength and ultimate axial strain of FRP-confined ECC columns. Compared with the existing design equations, the developed design equations can exhibit closer predictions with test results.

(5) Existing dilation models were used to generate the predictions on the lateral strain-axial strain curves for FRP-confined ECC, followed by the comparisons with test results. Yuan et al.'s model [25] developed based on the test data of FRP-confined ECC exhibits the better performance than the other models developed based on the FRP-confined normal concrete. It further demonstrates that the lateral dilation behavior of FRP-confined ECC is different from that of FRP-confined normal concrete.

(6) Existing analysis-oriented models were evaluated in this study for FRP-confined ECC. The higher predicted stress-strain curves compared with test results indicate that the analysis-oriented models developed based on FRP-confined normal concrete are not applicable to FRP-confined ECC. New analysis-oriented model was proposed for FRP-confined ECC, with the use of accurate dilation model and actively-confined model. Axial stress-axial strain curves predicted by the proposed analysis-oriented model can match can well with test results. Meanwhile, close agreements on the ultimate conditions could be obtained as well, which further demonstrates the good performance of the proposed analysis-oriented model.

It is worth noting that the analysis-oriented model proposed in this study could also be used to generate the envelope curve for FRP-confined ECC specimens under cyclic loading. Other components in the cyclic stress-strain model including the unloading/reloading curves, plastic strain and stress deterioration can be developed in the similar approach to FRP-confined normal concrete in future studies.

Acknowledgement

The research work presented in this paper was supported by the Research Grants Council of the Hong Kong Special Administrative Region, China – Theme-based Research Scheme (Project No. T22-502/18-R).

References

[1] Zhu JY, Chen J, Chan T-M. Analytical model for circular high strength concrete filled steel tubes under compression. Eng Struct 2021;244:112720.

[2] Hu JY, Zhang SS, Chen E, Li WG. A review on corrosion dsetection and protection of existing reinforced concrete (RC) structures. Constr Build Mater 2022;325:126718.

[3] Zhu JY, Chan T-M. Experimental investigation on steel-tube-confined-concrete stub column with different cross-section shapes under uniaxial-compression. J Constr Steel Res 2019;162:105729.

[4] Li VC, Wang S, Wu C. Tensile strain-hardening behavior of polyvinyl alcohol engineered cementitious composite (PVA-ECC). ACI Mater J 2001;98(6):483–92.

[5] Zhu JX, Xu LY, Huang BT, Weng KF, Dai JG. Recent developments in Engineered/Strain-Hardening Cementitious Composites (ECC/SHCC) with high and ultra-high strength. Constr Build Mater 2022;342:127956.

[6] Li VC. On engineered cementitious composites (ECC). J Adv Concr Technol 2003;1(3):215–30.

[7] Qin F, Zhang Z, Yin Z, Di J, Xu L, Xu X. Use of high strength, high ductility engineered cementitious composites. J Build Eng 2020;32:101746.

(ECC) to enhance the flexural performance of reinforced concrete beams

[8] Lee CK, Khan MKI, Zhang YX, Rana MM. Compressive performance of ECC-concrete encased high strength steel composite columns. Eng Struct 2020;213:110567.

[9] Khan MKI, Lee CK, Zhang YX. Numerical modelling of engineered cementitious composites-concrete encased steel composite columns. J Constr Steel Res 2020;170:106082.

[10] Chen X, Zhuge Y, Al-Gemeel AN, Xiong Z. Compressive behaviour of concrete column confined with basalt textile reinforced ECC. Eng Struct 2021;243:112651.

[11] Li F, Feng Z, Deng K, Yu Y, Hu Z, Jin H. Axial behavior of reinforced PP-ECC column and hybrid NSC-ECC column under compression. Eng Struct 2019;195:223-230.

[12] Dong B, Pan J, Cai J, Xu L. Mechanical behaviour of a new ECC-encased CFST column to RC beam connection under cyclic loading. Eng Struct 2021;234:111915.

[13] Qian H, Guo J, Yang X, Lin F. Seismic rehabilitation of gravity load-designed interior RC beam-column joints using ECC-infilled steel cylinder shell. Struct 2021;34:1212-1228.

[14] Wu LS, Yu ZH, Zhang C, Bangi T. Design approach, mechanical properties and cost-performance evaluation

of ultra-high performance engineered cementitious composite (UHP-ECC): A review. Constr Build Mater 2022;340:127734.

[15] Zhou J, Pan J, Leung CKY. Mechanical behavior of fiber reinforced engineered cementitious composites in uniaxial compression. J Mater Civ Eng 2015;27(1):04014111.

[16] Meng D, Huang T, Zhang YX, Lee CK. Mechanical behaviour of a polyvinyl alcohol fibre reinforced engineered cementitious composite (PVA-ECC) using local ingredients. Constr Build Mater 2017;141:259-270.

[17] Khan MKI, Rana MM, Zahng YX, Lee CK. Compressive behaviour of engineered cementitious composites and concrete encased steel composite columns. J Constr Steel Res 2020;167:105967.

[18] Xu SL, Cai XR. Experimental study and theoretical models on compressive properties of ultrahigh toughness cementitious composites. J Mater Civ Eng 2010;22(10):1067-1077.

[19] Ding Y, YU K, Mao W. Compressive performance of all-grade engineered cementitious composites: Experiment and theoretical model. Constr Build Mater 2020;244:118357.

[20] Pessiki S, Harries KA, Kestner JT, Sause R, Ricles JM. Axial behavior of reinforced concrete columns confined with FRP jackets. J Compos Constr 2001;5(4):237-245.

[21] Zhu JY, Lin G, Teng JG, Chan T-M, Zeng JJ, Li LJ. FRP-Confined square concrete columns with section curvilinearization under axial compression. J Compos Constr 2020;24(2):04020004.

[22] Ozbakkaloglu T, Vincent T. Axial compressive behavior of circular high-strength concrete-filled FRP tubes. J Compos Constr 2014;18(2):04013037.

[23] Sirach N, Smith ST, Yu T, Mostafa A. Experimental study on the confinement of concrete cylinders with large rupture-strain FRP composites. J Compos Constr 2021;25(4):04021026.

[24] Dang Z, Feng P, Yang JQ, Zhang Q. Axial compressive behavior of engineered cementitious composite confined by fiber-reinforced polymer. Compos Struct 2020;243:112191.

[25] Yuan WY, Han Q, Bai YL, Du XL, Yan ZW. Compressive behavior and modelling of engineered cementitious composite (ECC) confined with LRS FRP and conventional FRP. Compos Struct 2021;272:114200.

[26] Li S, Chan T-M, Young B. Behavior of GFRP-concrete double tube composite columns. Thin-Walled Struct 2022;178:109490.

[27] Teng JG, Huang Y, Lam L, Ye L. Theoretical model for fiber-reinforced polymer confined concrete. J Compos Constr 2007;11(2):201–10.

[28] Yang JQ, Feng P. Analysis-oriented models for FRP-confined concrete: 3D interpretation and general methodology. Eng Struct 2020;216:11074.

[29] ASTM C39-20. Standard test method for compressive strength of cylindrical concrete specimens. American Society for Testing and Materials, Philadelphia, USA, 2020.

[30] ASTM C469-14. Standard test method for static modulus of elasticity and Poisson’s ratio of concrete in compression. American Society for Testing and Materials, Philadelphia, USA, 2014.

[31] Japan Society of Civil Engineers. Recommendations for design and construction of high performance fiber reinforced cement composites with multiple fine cracks (HPFRCC). Concrete Engineering Series 82, 2008.

[32] ASTM D2290-08. Standard test method for apparent hoop tensile strength of plastic or reinforced plastic pipe by split disk method. American Society for Testing and Materials, Philadelphia, USA, 2008.

[33] ASTM D3039-17. Standard test method for tensile properties of polymer matrix composite materials. American Society for Testing and Materials, Philadelphia, USA, 2017.

[34] ASTM C192. Standard practice for making and curing concrete test specimens in the laboratory. American Society for Testing and Materials, Philadelphia, USA, 2019.

[35] Zhang B, Yu T, Teng JG. Behavior of concrete-filled concrete tubes under cyclic axial compression. J Compos Constr 2015;19(3):04014060.

[36] Lam L, Teng JG. Design-oriented stress-strain model for FRP-confined concrete. Constr Build Mater 2003;17(6):471–89.

[37] Lam L, Teng JG, Cheung CH, Xiao Y. FRP-confined concrete under axial cyclic compression. Cem Concr Compos 2006;28(10):949–58.

[38] Lam L, Teng JG. Stress–strain model for FRP-confined concrete under cyclic axial compression. Eng Struct 2009;31:308-321.

[39] Teng JG, Jiang T, Lam L, Luo YZ. Refinement of a design-oriented stress–strain model for FRP-confined concrete. J Compos Constr 2009;13(4):269-278.

[40] Concrete Society. Design guidance for strengthening concrete structures with fibre composite materials. Technical Rep. No. 55, 3rd Ed., Crowthorne, Berkshire, U.K. 2012.

[41] American Concrete Institute ACI. Guide for the design and construction of externally bonded FRP systems for strengthening concrete structures. ACI-440 2R, Farmington Hills, Mich. 2017.

[42] Cui C, Sheikh SA. Analytical model for circular normal- and high-strength concrete columns confined with FRP. J Compos Constr 2010;14:562-572.

[43] Liao J, Zeng JJ, Gong QM, Quach WM, Gao WY, Zhang L. Design-oriented stress-strain model for FRP-confined ultra-high performance concrete (UHPC), Constr Build Mater 2022;318:126200.

[44] CEN. Eurocode 2: Design of concrete structures – Part 1-1: General rules for buildings. EN 1993-1-1, European Committee for Standardization (CEN), Brussels, 2004.

[45] Li Y, Wang W, Wen C. Experiment study on mechanical performance of ECC under conventional triaxial compression. Concrete 2016;1:59–63 (in Chinese).

[46] Jiang T, Teng JG. Analysis-oriented stress-strain models for FRP-confined concrete. Eng Struct 2007;29:2968-2986.

[47] Lim JC, Ozbakkaloglu T. Unified stress-strain model for FRP and actively confined normal-strength and high-strength concrete. J Compos Constr 2015;19(4):04014072.

[48] Lai MH, Liang YW, Wang Q, Ren FM, Chen MT, Ho JCM. A stress-path dependent stress-strain model for FRP-confined concrete. Eng Struct 2020;203:109824.

[49] Popovics, S. A numerical approach to the complete stress-strain curve of concrete. Cement and Concrete Research, 1973;3:583-599.

[50] Yang JQ, Feng P. Analysis-oriented model for FRP confined high-strength concrete: 3D interpretation of path dependency. Compos Struct 2021;278:114695.